Water Science & Technology

Water Science & Technology Vol 94 No 1, 123 doi: 10.2166/wst.2026.297

Application of flood hazard assessment for decision-making in the White Volta Basin, Ghana

Samuel Owusu Ansah [a,b,*], Yakob Umer [c], Thompson Annor [a], Andrew Manoba Limantol [d], Isaac Larbi [d], Babatunde Abiodun [e], Joshua Asamoah [a,b], Alfred Awuah [a,f] and Meron Teferi Taye [g]

[a] Department of Meteorology and Climate Science, Kwame Nkrumah University of Science and Technology (KNUST), Kumasi, Ghana
[b] Ghana Meteorological Agency, 485-3581 Accra, Ghana
[c] International Water Management Institute, Pretoria, South Africa
[d] School of Sustainable Development, University of Environment and Sustainable Development, Somanya, Ghana
[e] Nansen-Tutu Centre for Marine and Environmental Research, Department of Oceanography, University of Cape Town, Cape Town, South Africa
[f] Department of Environmental Management and Technology, Koforidua Technical University, Koforidua, Ghana
[g] International Water Management Institute, East Africa and Nile Basin Office, Addis Ababa, Ethiopia
*Corresponding author. E-mail: ansahsamuelowusu2014@gmail.com

SOA, 0000-0001-5375-8876; YU, 0000-0002-7325-3450; TA, 0000-0003-0686-2827; AML, 0000-0002-7359-7616; IL, 0000-0001-8748-0649; BA, 0000-0002-3878-0116; JA, 0009-0008-2358-640X; AA, 0009-0006-6571-3310; MTT, 0000-0002-4687-4622

ABSTRACT

Flooding is a major natural hazard in Ghana, with the White Volta Basin (WVB) highly susceptible due to flat terrain, intense rainfall, and upstream dam releases. The September 2020 flood, caused by heavy rainfall and Bagre Dam spillage, inundated croplands and settlements, revealing the need for impact-based flood intelligence. This study uses the Hydrologic Engineering Center's River Analysis System to simulate flood dynamics and assess cropland exposure. Calibration and validation with Sentinel-1 Synthetic Aperture Radar-derived flood extent showed strong spatial agreement (61–77%). A composite flood hazard index, combining water depth and velocity, classified hazard intensity into seven levels, linking hydraulic severity with crop impacts. The framework guides community-level early warning and preparedness, supporting decision-making by the National Disaster Management Organization (NADMO), Ministry of Food and Agriculture (MoFA), Water Resources Commission (WRC), and Ghana Meteorological Agency (GMet). High-risk areas included Bawku West (22.7%), Binduri (15.1%), and Talensi (6.1%), aiding climate-resilient planning in transboundary basins.

Key words: 2D hydraulic modelling, flood hazard index, flood risk mapping, HEC-RAS, White Volta Basin cropland exposure

GRAPHICAL ABSTRACT

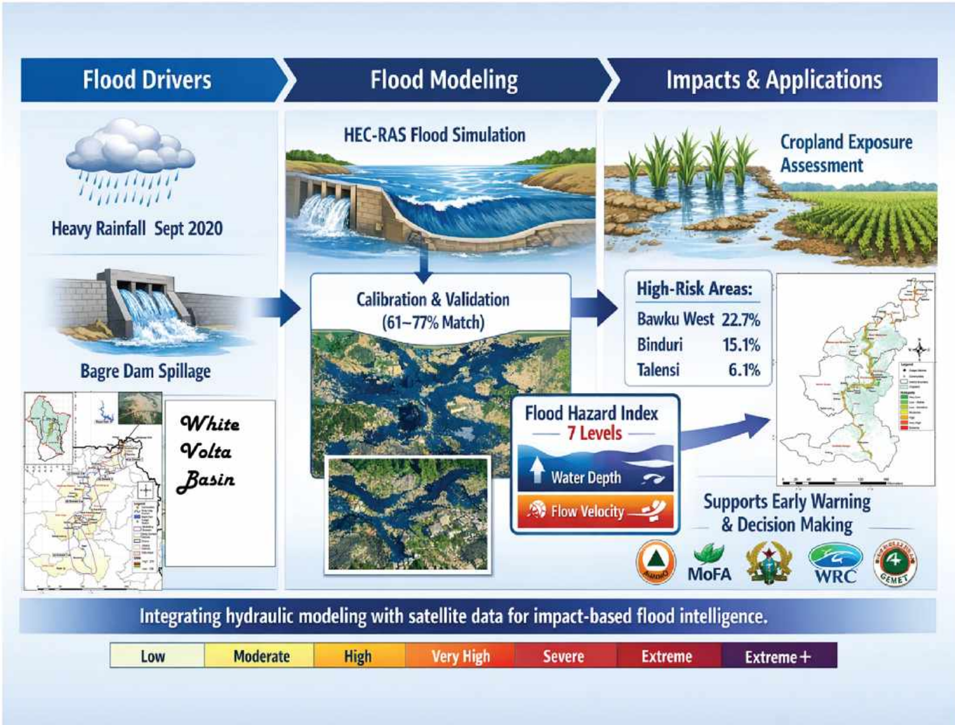

1. INTRODUCTION

Flooding is a devastating global hazard that continues to cause widespread damage to infrastructure, livelihoods, and ecosystems (Glago 2021). In West Africa, this threat is particularly acute, with Ghana experiencing recurrent floods that disrupt socio-economic stability, displace communities, and undermine food security (Atanga & Tankpa 2021; Atubiga & Donkor 2022; Arhin & Frimpong 2025; Kwarteng *et al.* 2025). The White Volta Basin (WVB) has a long history of severe flooding, with catastrophic events in 2007, 2009, and 2010 affecting hundreds of thousands of people, destroying homes, and inundating farmlands extensively (Yiran & Stringer 2016; Fiasorgbor *et al.* 2018). These events highlight not only the exposure of settlements and infrastructure but also the high vulnerability of cropland, which amplifies risks to rural livelihoods and national food security. Fiasorgbor *et al.* (2018) reported that the August 2007 floods were the worst recorded in the Builsa District, resulting in three human fatalities and widespread property loss, with over 1,300 households rendered homeless. Many buildings were submerged, and more than 3,000 ha of farmland were destroyed. The basin's susceptibility is further intensified by multiple interacting drivers: intense seasonal rainfall, deforestation, agricultural expansion, and upstream dam releases from the Bagre reservoir (Smits *et al.* 2024). Such dynamics result in floodwaters that persist across farmlands, leading to crop mortality, soil erosion, and declining agricultural productivity. Consequently, assessing agricultural exposure is central to understanding the full scope of flood risk in the WVB, where livelihoods are predominantly agrarian.

Effective flood mitigation and early warning depend on reliable hydrodynamic modelling that accurately reproduces flood dynamics. The Hydrologic Engineering Center's River Analysis System (HEC-RAS) has proved effective in simulating flood dynamics across diverse hydrological contexts from humid tropical basins in Benin to major floodplains in Pakistan and India (Afzal *et al.* 2022; Amoussou *et al.* 2024). In Ghana, its application has been demonstrated in the Lower Volta Basin (Logah *et al.* 2017). However, operational deployment of a calibrated and validated HEC-RAS model for the WVB remains limited, constrained by coarse data resolution, insufficient event-based calibration, and transboundary hydrological complexity. While models such as the LISFLOOD Floodplain Inundation Model and SOBEK Integrated Hydrodynamic Modelling Suite have been applied in neighbouring basins (Komi *et al.* 2017; Willis *et al.* 2022), a rigorously validated and context-specific hydraulic model for the WVB is still lacking.

Translating flood simulations into decision-relevant information remains a persistent gap in risk management. While conventional maps often focus solely on inundation extent, they overlook the combined influence of flow velocity and duration, critical determinants of crop damage. This study addresses this limitation by developing a composite flood hazard index (HI) that integrates flood depth and flow velocity into a unified, operationally interpretable framework. Although flood duration is conceptually significant, the high-resolution spatial and temporal data required to quantify it consistently across the study area were unavailable. Consequently, the HI prioritises the depth–velocity interaction, providing a hazard classification that aligns with observable field impacts on local croplands and settlements.

The motivation for categorising HI into multiple levels stems from the need to bridge technical modelling outputs with formal decision-making support. In this context, decision-making support refers to an operational framework that translates complex hydraulic parameters into evidence-based triggers for disaster response and spatial planning. Each hazard level conveys actionable meaning: for example, low-HI zones may indicate moisture recharge areas, while very high-HI zones denote destructive flooding requiring anticipatory action (AA), seed support, or evacuation. This approach enhances coordination between agencies such as NADMO, MoFA, WRC, and GMet by linking hydraulic severity to locally relevant response thresholds.

The primary objective of this study is to generate actionable, impact-based flood intelligence. Specifically, it seeks to model the September 2020 flood event using HEC-RAS, validated against Sentinel-1 Synthetic Aperture Radar (SAR)-derived flood extents; develop a composite HI integrating depth and velocity to classify hazard severity; and quantify cropland exposure to identify high-risk zones while establishing a science-to-policy framework for climate-resilient planning and disaster risk reduction.

2. MATERIALS AND METHODS

2.1. Study area

The study area, illustrated in Figure 1, is located in the north-eastern corridor of Ghana and spans the Upper East, North East, Northern, and Savannah regions. The research focuses on a major reach of the White Volta River, which flows southward from the Ghana–Burkina Faso border. This river forms the principal hydrological artery of the WVB, a key sub-basin of the Volta River Basin, covering approximately 107,417 km^2 across northern Ghana and Burkina Faso (Barry *et al.* 2005). Topographically, the basin is characterised by a generally flat and low-lying landscape, with elevations between 200 and 300 m above sea level. The gentle relief, highlighted by the digital elevation model (DEM) in Figure 1, increases the susceptibility of the area to flooding during periods of intense rainfall or upstream dam releases (Atubiga & Donkor 2022). The basin also hosts about 254 small reservoirs, which serve as critical water sources during the prolonged dry season (Ghansah *et al.* 2018).

Climatically, the WVB exhibits a tropical regime with distinct wet and dry seasons. The rainy season (June–October) produces peak flows and significant flood risks, while the long dry season (November–May) is characterised by low flows and heavy reliance on stored water. These seasonal contrasts, combined with the operational dynamics of the Bagre Dam in Burkina Faso, shape the basin's hydrological dynamics and drive its flood vulnerability (Fiasorgbor *et al.* 2018; Smits *et al.* 2024).

This vulnerability was starkly demonstrated during the September 2020 flood event, when heavy rainfall combined with controlled spillage from the Bagre Dam caused extensive inundation across large sections of the basin. The flood covered an estimated area of approximately 10,000 km^2, severely affecting communities, infrastructure, and agricultural lands. For this study, the river reach was divided into five analytical domains, i.e., 717.3, 841.5, 1,128.8, 3,486.8, and 4,094.0 km^2 for Domains 1–5, respectively, to support a more detailed assessment of flood hazard, exposure, and vulnerability at the district scale. Together, these domains represent a total area of 10,268.5 km^2, which is consistent with the approximate extent of the 2020 flood event.

2.2. Data used

2.2.1. Flow data

Streamflow data used in the HEC-RAS hydraulic simulations were obtained from three primary gauging stations along the White Volta River (WVB): Yarigu, Pwalugu, and Daboya. The Yarigu station provides continuous daily discharge records from 1998 to 2020, Pwalugu offers a longer historical dataset spanning 1963–2023, and Daboya covers 2000–2020. While these observed datasets are valuable, they remain limited in both spatial and temporal coverage. Large portions of the WVB remain ungauged, and even at existing stations, data gaps occur due to equipment malfunction, accessibility

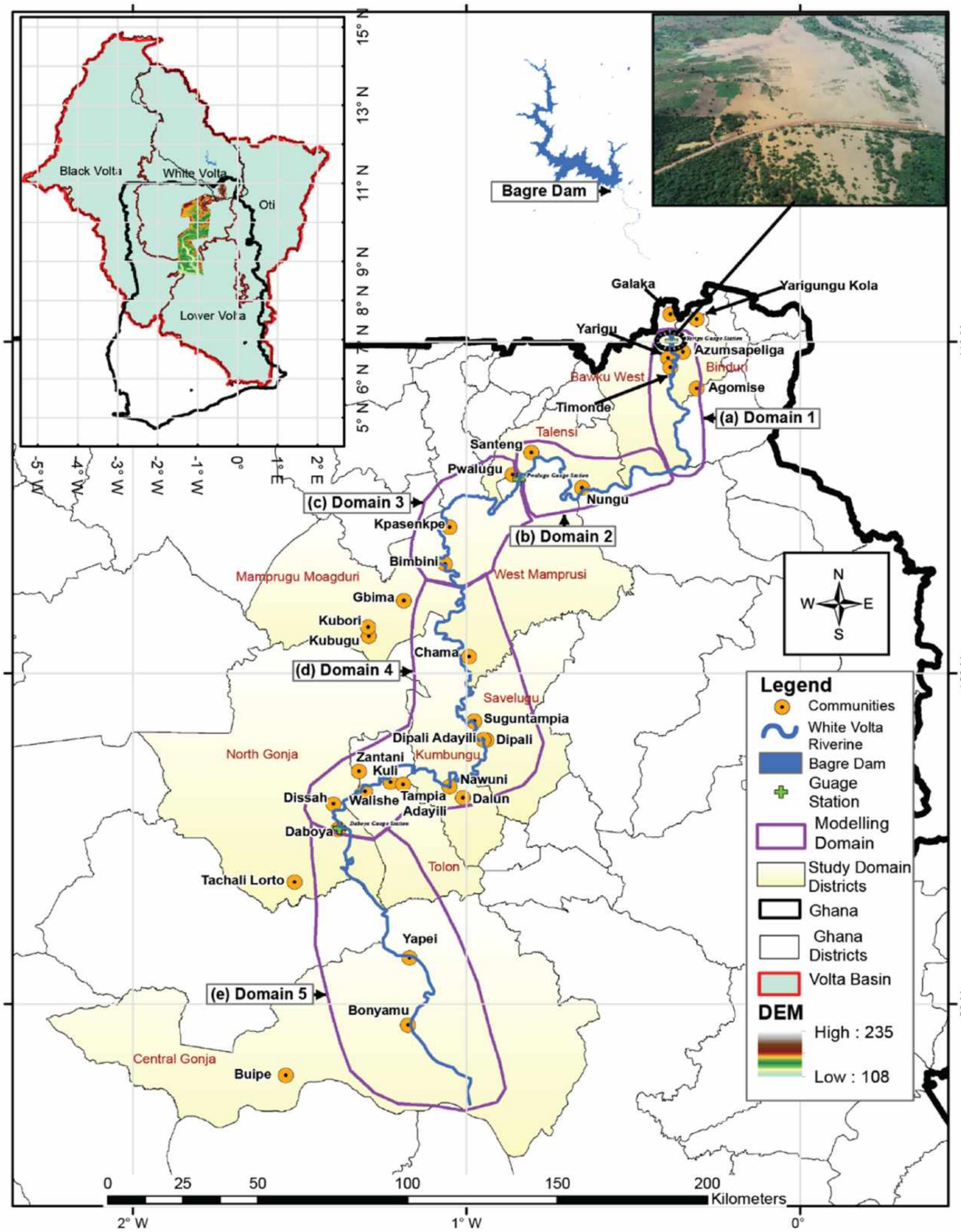

Figure 1 | Location of the study area within the Volta Basin, Ghana, showing the five hydraulic modelling domains (Domains 1–5), administrative districts, major river networks, and selected communities. Background shading represents regional topography derived from a DEM.

constraints, and incomplete records. Furthermore, discharge gauges measure streamflow only at single points along the river and therefore cannot capture the spatial distribution of flooding, such as inundation extent, depth, or flood progression across the floodplain. To address these limitations, satellite-based flood observations were incorporated to complement the point-based gauge data.

In the hydraulic model, the observed discharge records were used to define the upstream boundary conditions, meaning the volume of water entering the model domain that initiates and drives flow movement through the simulated river system. This serves as the starting hydraulic input required for flood simulations. Meanwhile, satellite-derived flood inundation maps provided spatially continuous information used for model calibration and validation, ensuring that simulated inundation patterns aligned with observed flood extents.

The discharge datasets also supported flood frequency analysis for scenario development. Prior to use, the daily time series underwent rigorous quality control, including screening for anomalies and filling missing values through established techniques such as linear interpolation and correlation-based estimation with nearby stations (Dembélé *et al.* 2019; Dembélé *et al.* 2020). Hydrographs from Yarigu, Pwalugu, and Daboya during the August–September 2020 flood season are presented in Figure 2, respectively. These visualisations highlight the temporal variability in discharge during the peak flooding period and serve as essential inputs for model simulation.

2.2.2. DEM

A DEM provided by FUGRO NPA Limited was utilised to support multiple components of the HEC-RAS hydraulic modelling framework. The DEM was derived from SPOT high-resolution stereoscopic satellite imagery and provided a spatial resolution of 20 m appropriate for detailed flood analysis. It was projected in WGS_1984_UTM_Zone_30N, with the vertical reference aligned to the Ghanaian National Level Datum (NLD). The archived DEM featured an absolute elevation accuracy of 10 m (90% confidence for terrain slopes less than 20°) and a planimetric accuracy of 15 m (90% confidence). To improve vertical accuracy, 23 pairs of ground control points (GCPs) were collected through field surveys. These GCPs were used to perform a vertical adjustment, enhancing the alignment of the DEM with real-world terrain and improving the reliability of terrain inputs for both the one-dimensional (1D) and two-dimensional (2D) HEC-RAS model components.

2.2.3. Satellite flood inundation

This study employs the Sentinel-1 mosaic product, derived from ESA's C-band SAR imagery, to support flood monitoring and hazard assessment in the WVB. Sentinel-1's all-weather, day-and-night imaging capability enables consistent surface observations despite the persistent cloud cover and intense rainfall typical of tropical regions. With a 6-day revisit time (~3-day effective data availability) and a spatial resolution of 10 m, the product provides timely and detailed information

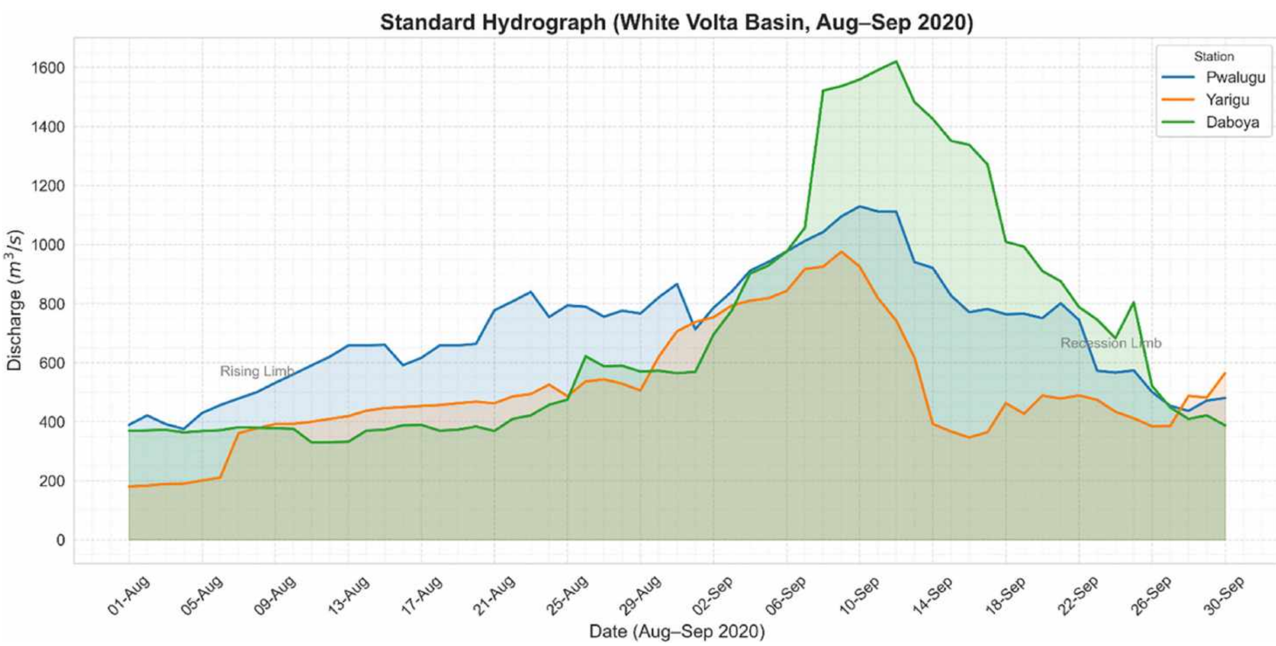

Figure 2 | Hydrograph depicting daily discharge variations at Pwalugu, Yarigu, and Daboya stations in the White Volta Basin during August–September 2020, highlighting the rising and recession limbs, with peak flows observed in early September, corresponding to the major flood event across the basin.

on flood extent. In this study, satellite-derived flood inundation maps were used for both the calibration and validation of the hydrodynamic model, ensuring that simulated flood extents realistically reflected observed inundation patterns. Five flood domains (Figure 1) were mapped using multi-temporal Sentinel-1 mosaics for the period 2017–2024 within the Google Earth Engine environment. These datasets were analysed to determine the relative severity of annual flood events, expressed as the percentage of inundated area (Figure 4). The use of multi-temporal Sentinel-1 mosaics also facilitated time-series flood analysis, enabling the tracking of flood evolution across key dates. This approach supported the identification of the onset, peak, and recession phases of the 2020 flood event. However, the 6-day repeat cycle presents a limitation, as rapid flood dynamics may not always be captured. Water may recede into the channel before the next satellite overpass, potentially leading to underestimation or misrepresentation of the true extent of flooding (Braun 2021).

2.2.4. Flood history from NADMO

Historical flood records obtained from the National Disaster Management Organization (NADMO) provided valuable insights into the frequency, causes, and spatial distribution of flood events between 2017 and 2024 (Table 1). The documented triggers included torrential rainfall and controlled spillage from the Bagre Dam. The records also distinguished between field-reported events and satellite-based observations, underscoring the increasing role of remote sensing in flood monitoring. In this study, the NADMO database, focusing specifically on the extensive 2020 flood event that occurred between August 15 and October, was analysed to identify the most affected district cropland, correlate the timing of flooding with reported triggers, and establish a baseline understanding of the event's characteristics.

2.2.5. Land use/land cover

This study employed two global land use and land cover (LULC) datasets, i.e., Esri 2020 Land Cover and ESA World Cover 2020, to estimate cropland exposure to flooding in the WVB. Both products provide 10 m spatial resolution but differ in their underlying inputs. The Esri dataset is derived from Sentinel-2 optical imagery using machine-learning classification, whereas ESA World Cover integrates Sentinel-1 SAR and Sentinel-2 optical imagery through a random forest classifier (De Luca *et al.* 2022). Using both datasets helped reduce uncertainty, as global LULC products exhibit variable cropland accuracy across heterogeneous landscapes (Pérez-Hoyos *et al.* 2017). Assessment of the two datasets showed that the Esri product performed well in districts such as Bawku West, Binduri, and Talensi, where cropland is spatially contiguous, but it under-represented cropland in more fragmented landscapes. In such areas, greater reliance was placed on ESA World Cover, which provided a more consistent basin-wide representation. Both datasets are limited by potential misclassification in smallholder, mixed-farming systems and by their inability to capture seasonal land-surface dynamics such as fallow and actively cultivated

Table 1 | Historical flood events (2017–2024) in the Talensi District, Ghana, showing dates, primary causes, and affected communities

Date	Disaster type	Cause	Location
29 August–17 September 2017	Floods	Torrential rains	Pwalugu, Guborigu, Yinduri, Santeng, Biung, Nungu, Bapella, Tolla, and Degaare
11 August–30 September 2018	Floods	Bagre Dam/ torrential rains	Pwalugu, Guborigu, Yinduri, Santeng, Biung, Nungu, Bapella, Winkogo, Baare, Vung, Balungu, Yale, Tolla, and Degaare
12 September–21 October 2019	Floods	Torrential rains	District wide
15 August–17 September 2020	Floods	Bagre Dam/ Torrential rains	Pwalugu, Guborigu, Yinduri, Santeng, Biung, Nungu, Bapella, Winkogo, Balungu, Kulpelga, Namoranteng, Yale, Tolla, and Degaare
19–31 August 2021	Floods	Torrential rains	Pwalugu, Yinduri, Guborigu, Santeng, Biung, Nungu, Bapella, Tolla, and Degaare
4 September–12 October 2022	Floods	Bagre Dam/ torrential rains	Pwalugu, Yinduri, Santeng, Biung, Nungu, Bapella, Tolla, and Degaare
19 August–3 September 2023	Floods	Bagre Dam/ torrential rains	Pwalugu, Guborigu, Yinduri, Santeng, Biung, Nungu, Bapella, Tolla, and Degaare
21 August–9 September 2024	Floods	Bagre Dam/ torrential rains	Pwalugu, Guborigu, Yinduri, Santeng, Biung, Nungu, Bapella, Vung area, Winkogo, Balungu, Yale, Tolla, and Degaare

fields. Validation using Google Maps high-resolution imagery confirmed these differences: in Bawku West, Esri accurately mapped cropland patterns, whereas in West Mamprusi, it misclassified substantial areas that ESA World Cover correctly identified. Beyond exposure analysis, the LULC datasets were incorporated into the HEC-RAS 2D hydrodynamic model to assign spatially distributed Manning's roughness coefficients, a key parameter controlling flow resistance, velocity attenuation, inundation extent, and flood duration. Land-cover classes (cropland, savannah, forest, built-up areas, and water bodies) were converted into roughness zones, with higher Manning's n values assigned to dense vegetation and built-up surfaces and lower values to open cropland and grassland. This parameterisation improved the physical realism of flood simulations by ensuring that hydraulic behaviour reflected underlying land-surface conditions, thereby enhancing the robustness and reliability of the overall flood analysis.

2.3. Methodology

2.3.1. Flood frequency analysis

Flood frequency analysis was conducted using the generalised extreme value (GEV) distribution, a widely accepted method for modelling annual maximum discharge data. This approach allows for estimation of return levels (e.g., 5-, 10-, 25-, 50-, and 100-year floods) critical for hydraulic modelling and infrastructure planning.

Annual peak discharge values recorded at the Yarugu, Pwalugu, and Daboya streamflow gauging stations from 1998 to 2020, 1963 to 2023, and 2000 to 2020, respectively, were utilized for this analysis. The GEV distribution, which encompasses the Gumbel, Fréchet, and Weibull families as special cases, is suited for capturing the statistical behaviour of extreme hydrological events. Parameters of the GEV distribution location (μ), scale (σ), and shape (ξ) were estimated using the maximum likelihood estimation (MLE) method.

Goodness-of-fit tests, including the Anderson–Darling (A–D) and Kolmogorov–Smirnov (K–S) statistics, were applied to verify the suitability of the GEV model for the discharge dataset. Return period (RP) discharges were then computed, forming the basis for defining boundary conditions and simulating design floods within the HEC-RAS hydraulic model:

$$F(x) = \exp\left\{-\left[1 + \xi\left(\frac{x-\mu}{\sigma}\right)\right]^{-1/\xi}\right\},\ 1 + \xi\left(\frac{x-\mu}{\sigma}\right) > 0 \tag{1}$$

where x = annual maximum discharge, μ = location parameter, $\sigma > 0$ = scale parameter, and ξ = shape parameter. Parameters (μ, σ, ξ) were estimated using the MLE method, and the model performance was evaluated using goodness-of-fit tests based on the A–D and K–S statistics.

Finally, the resulting return levels were mapped to identify communities most exposed to frequent and high-magnitude flood events, supporting flood risk assessments and early warning system development across the basin.

2.3.2. Flood model setup: HEC-RAS

The methodology for developing floodplain maps (Figure 3) employed a flood modelling framework that combined observed discharge data, a DEM, flood frequency analysis, and hydraulic simulations. First, design floods corresponding to various RPs (e.g., 10, 50, and 100 years) were estimated from observed discharge data using flood frequency analysis. A high-resolution SPOT DEM was acquired and processed to provide the topographic foundation for the modelling framework. SPOT DEMs are generated from imagery obtained by the French Satellite Pour l'Observation de la Terre (SPOT) series and offer a spatial resolution of approximately 20 m, enabling a detailed and accurate representation of the Earth's surface elevation for hydrological analysis and flood modelling. Subsequently, model domain meshes were generated to characterise the river reach and define the modelling domain.

For hydraulic modelling, river reach features such as centrelines, banks, and cross-sections were extracted from the DEM using the RAS Mapper tool in HEC-RAS. A 2D HEC-RAS model was then configured to capture floodplain processes, incorporating hydraulic structures that were available, Manning's roughness coefficients derived from land cover classifications, and appropriate upstream and downstream boundary conditions. Key geometric datasets, including the 2D flow area mesh, were generated from the SPOT DEM, and effective roughness regions were defined in GIS and integrated via the RAS Mapper interface (Horritt & Bates 2002; Schumann *et al.* 2009). The inflow hydrographs for the 2D model were derived from observed flood events and applied as unsteady flow inputs, while a normal depth boundary condition based on channel slope and representative roughness was specified as the downstream outlet.

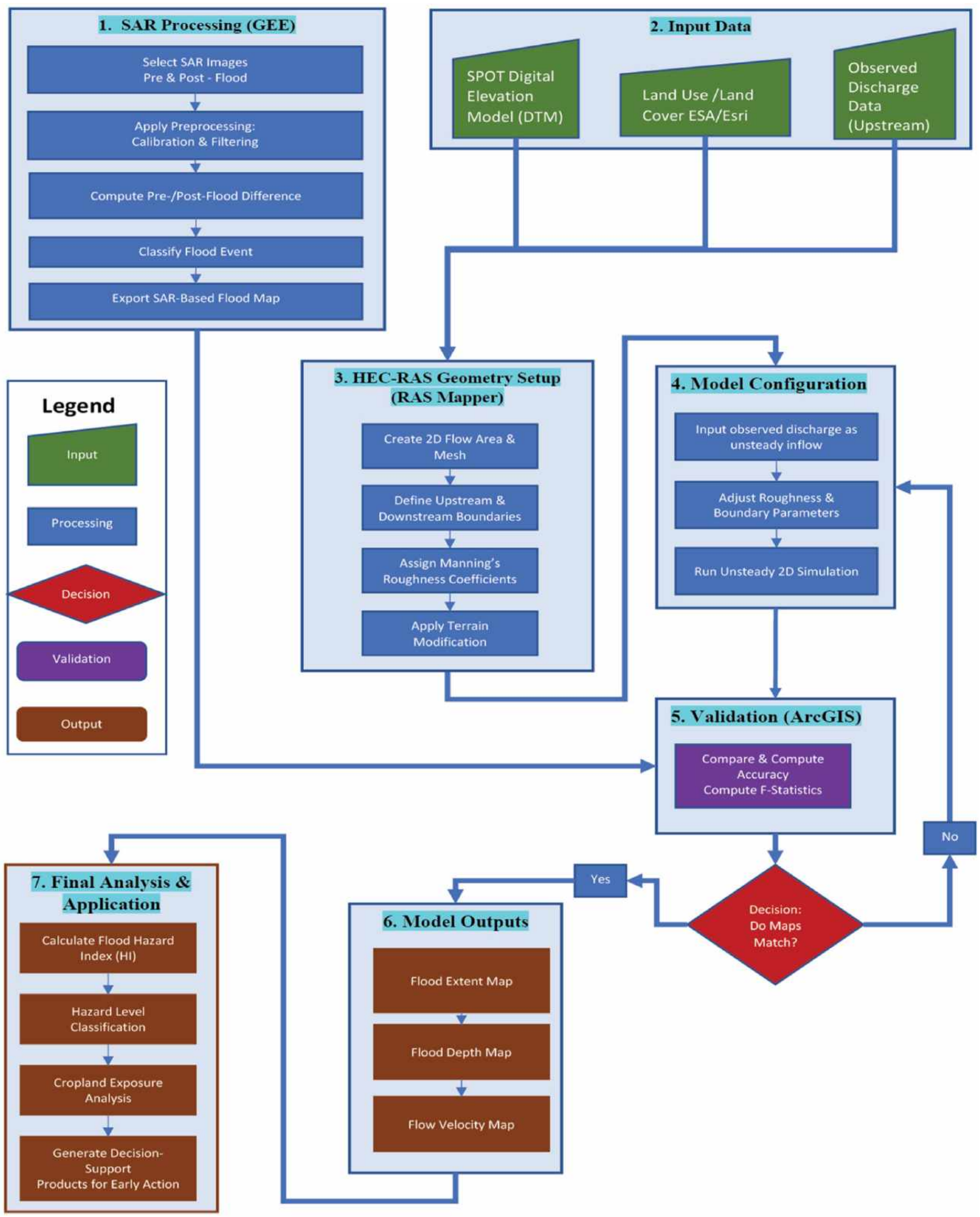

Figure 3 | Workflow for hydraulic modelling and flood hazard mapping using HEC-RAS 2D and Sentinel-1 data.

Simulations were performed in HEC-RAS to reproduce unsteady flow dynamics across the WVB. Model calibration and validation were carried out against observed discharge records for the August–September 2020 period, where available, together with historical flood extent data. This process included iterative adjustments of Manning's roughness values to minimise discrepancies between simulated and observed flood characteristics. The final calibrated model was used to simulate design flood scenarios, producing outputs such as water surface elevations, inundation extents, depth grids, and velocity fields. The HEC-RAS, developed by the U.S. Army Corps of Engineers, supports both 1D and 2D modelling under steady and unsteady flow conditions (USACE 2016; Brunner 2023). In this study, the 2D modelling approach was adopted to more accurately capture overbank flow and floodplain interactions. Despite certain limitations, such as DEM resolution, simplification of roughness parameterisation, and limited validation datasets, the methodology provided a reliable representation of flood dynamics in the study area. The model outputs, including inundation maps and hydraulic indicators, form a critical basis for flood hazard and risk assessments in the WVB (Apel *et al.* 2009; Di Baldassarre *et al.* 2010; Teng *et al.* 2017).

2.3.3. Flood model validation using pixel-by-pixel statistics and visual comparison

The model's flood inundation outputs were evaluated by comparing them with a satellite-derived flood extent map generated from Sentinel-1 SAR imagery. For the 27 August 2020 event, a Sentinel-1 GRD scene covering the study area was available and processed to extract the observed flood extent. The mapping procedure involved radiometric calibration, speckle filtering, and conversion to backscatter coefficients, followed by threshold-based classification to distinguish water from non-water surfaces. The classified water mask was then refined using terrain data to remove false positives. Model validation was carried out using two complementary approaches. First, a visual comparison was performed by overlaying the simulated flood extent with the processed Sentinel-1 flood map to qualitatively assess spatial agreement. Second, a pixel-by-pixel accuracy assessment was undertaken using a contingency table to quantify hits, misses, and false alarms. For both assessments, the model was run for the same period as the satellite acquisition date to ensure temporal consistency. The agreement between simulated and observed flood extents was summarised using the *F*-statistic:

$$F = \frac{D}{B + C + D} \tag{2}$$

where B, C, and D are pixel counts defined in Table 2.

This equation calculates the proportion of correctly predicted wet pixels relative to the total number of flood-affected pixels. It excludes correctly predicted dry pixels to avoid bias introduced by domain size, since in large domains, many pixels are typically dry, which could falsely inflate accuracy. The *F*-statistic ranges from 0, indicating no overlap between satellite and simulated flood extents, to 1, representing perfect agreement.

2.3.4. HI

This metric serves as an indicator of cropland vulnerability by quantifying the physical severity of flooding on agricultural land. The Australian Rainfall and Runoff Guidelines (Rahman *et al.* 2015) define flood HI as a combined measure of floodwater depth and flow velocity, capturing their joint contribution to damage potential. Flood hazard intensity is computed as:

$$\mathrm{HI} = \mathrm{depth} \times \mathrm{velocity} \tag{3}$$

where depth (m) is the floodwater depth at a location and velocity (m/s) is the flow speed at the same location. To evaluate the degree of exposure of croplands, the HI values extracted specifically over cropland pixels are classified into three hazard levels:

Low: $\mathrm{HI} < 0.5\ \mathrm{m^2/s}$,
Medium: $0.5 \leq \mathrm{HI} < 1.0\ \mathrm{m^2/s}$, and
High: $\mathrm{HI} \geq 1.0\ \mathrm{m^2/s}$.

Table 2 | Contingency table used to define pixel-wise comparison metrics between model-simulated and observed flood extents

	Observed = dry	Observed = wet
Model = dry	A = dry/dry	B = predicted dry but observed wet
Model = wet	C = predicted wet but observed dry	D = wet/wet

These thresholds are used to generate a cropland hotspot class, which categorises the vulnerability of each cropland pixel as follows:

$$\text{cropland hotspot class} = \begin{cases} 1, & \text{if cropland}_{\text{HI}} < 0.5 \\ 2, & \text{if } 0.5 \geq \text{cropland}_{\text{HI}} < 1.0 \\ 3, & \text{if cropland}_{\text{HI}} \geq 1.0 \end{cases} \tag{4}$$

This classification enables the identification of cropland areas most susceptible to flood impacts, supporting targeted assessment of agricultural risk (Dutta *et al.* 2003; Rahman *et al.* 2015).

2.3.5. Cropland exposure level

The cropland exposure level quantifies the proportion of agricultural land affected by flooding within a given district. It is computed as:

$$\text{exposure level (\%)} = \frac{\text{cropland area exposed to flood}}{\text{total cropland area of district}} \times 100 \tag{5}$$

The assessment is performed on a pixel-by-pixel basis using the cropland raster dataset. First, cropland pixels that spatially intersect with the modelled or observed flood extent are identified. The sum of these intersecting cropland pixels represents the cropland area exposed to flood (km^2 or ha). The total cropland area of the district is obtained by summing all cropland pixels within the administrative boundary.

This pixel-level approach ensures that exposure is calculated with high spatial precision rather than treating the cropland shapefile as a single aggregated unit.

3. RESULTS AND DISCUSSION

3.1. Satellite-derived flood inundation (2017–2024)

Figure 4 presents a multi-year overview of flood dynamics and their impact on cropland in the WVB of Ghana, with specific emphasis on the riverine corridor of the WVB across five model domains where continuous Sentinel-1 data are available. The depiction of both flooded areas and flooded cropland (in hectares) from 2017 to 2024 provides valuable insights into the recurrent nature of flood hazards along the river system and their direct implications for food security and rural livelihoods in this vulnerable floodplain environment. A notable feature of this temporal analysis is the sharp rise in both total flooded area and, critically, flooded cropland during 2020. While interannual fluctuations are evident, the pronounced surge in 2020 highlights the severity of flooding in that year, corroborating NADMO reports describing a prolonged flood episode between August and September 2020.

The persistence of flooded cropland across all domains throughout the study period underscores the chronic threat that riverine flooding poses to agricultural resilience and local economies in the WVB. Overall, Sentinel-1 observations show that flood extent peaked in 2020, with an average inundation of 19% (75,956 ha), whereas 2017 recorded the lowest extent at just 7% (27,233 ha). This variability highlights the fluctuating nature of riverine flood impacts over time and their continuing significance for agricultural sustainability in the region as events are becoming more extreme.

3.2. Model validation: pixel-by-pixel comparison for the 2020 flood event

Model validation was conducted using two complementary approaches, reflecting the different types of observed data available across the study area. First, where discharge gauging stations were present (Domains D1, D3, and D5), simulated water levels and flows were compared with observed discharge records to ensure that the hydrodynamics of the model were consistent with measured river conditions. Second, to evaluate the accuracy of simulated flood extent, a spatial validation was performed by comparing modelled inundation maps with satellite-derived flood extents from Sentinel-1 imagery. For the spatial validation, contingency metrics (hits, false alarms, and misses) were computed using a pixel-by-pixel comparison, from which fuzzy accuracy was derived to account for uncertainty along flood boundaries (Aronica *et al.* 2002; Stephens *et al.* 2014). As shown in Table 3, Domain 1 achieved a fuzzy accuracy of 61.47%, with 417,989 hits, 243 false alarms, and 2,617 misses. Domain 3 showed the strongest performance, attaining 76.91% fuzzy accuracy with over 1,015,212

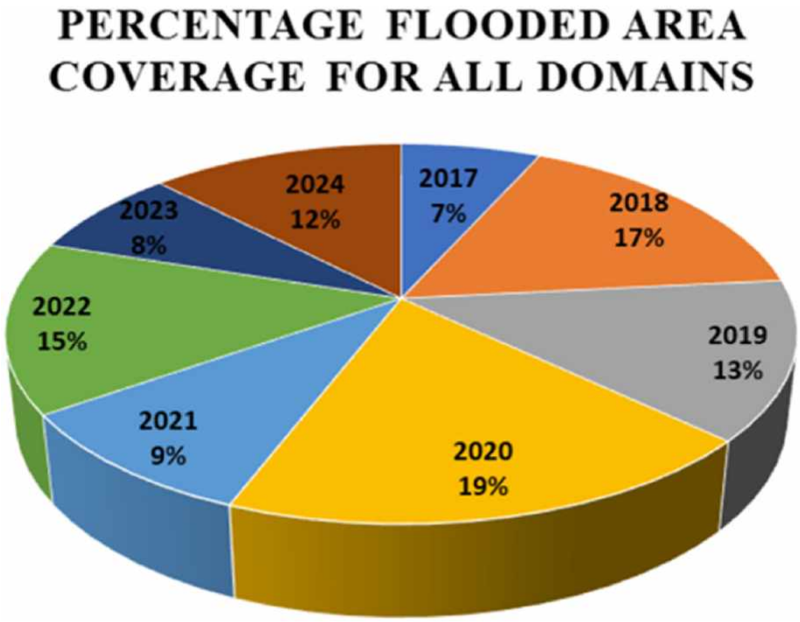

Figure 4 | Percentage distribution of total flooded area across years (2017–2024) for Domain 1, Domain 2, Domain 3, Domain 4, and Domain 5 based on Sentinel-1 satellite observations. The pie charts illustrate interannual variations in flood extent, highlighting peak flooding in 2020 across all domains, with comparatively lower flood coverage in 2017.

Table 3 | Flood model accuracy metrics for Domains 1, 3, and 5 showing hits, false alarms, misses, and fuzzy accuracy (%)

Contingency metrics	Domain 1 no. pixels	D1 fuzzy accuracy (%)	Domain 3/no. pixels	D3 fuzzy accuracy (%)	Domain 5/no. pixels	D5 fuzzy accuracy (%)
Hit	417,989	61.47	1,015,212	76.91	11,369,224	63.92
False alarm	243		8,327		16,369	
Misses	2,617		296,548		625,477	

hits, though accompanied by 296,548 misses and 8,327 false alarms. In contrast, Domain 5, a larger and more heterogeneous area, recorded 63.92% fuzzy accuracy, with 11,369,224 hits, 16,369 false alarms, and 625,477 misses.

These results show that model accuracy varies with domain size and landscape complexity. The higher performance in D3 suggests better representation of inundation processes, whereas D1 and D5 exhibit localised over- and under-estimations. Overall, the combined discharge-based and satellite-based validation demonstrates that the model reliably reproduces observed flood behaviour across the study area (Horritt & Bates 2002; Schumann *et al.* 2009).

The spatial accuracy, also shown in Figure 5 of flood model performance across Domains 1, 3, and 5, was evaluated using a pixel-by-pixel contingency approach. In this assessment, correctly predicted flooded pixels (hits) are represented in red, while overpredicted areas (false alarms) appear in purple, and missed flooded pixels (misses) are shown in white. A DEM background is included to provide topographic context, illustrating how terrain influences the spatial distribution of flooding.

3.3. Cropland exposure during the 2020 flood event

Cropland exposure to flooding in the WVB was evaluated by comparing observed flood extents derived from Sentinel-1 SAR imagery with simulated flood extents generated by the HEC-RAS 2D model for the 2020 flood event (Figure 6). The Sentinel-1-based inundation map represents the observed extent of flooding, while the HEC-RAS output provides the simulated flood footprint. The comparison shows substantial inundation along the river corridor, including significant impacts on adjacent croplands. District-level analysis revealed spatial variability, with the HEC-RAS model generally producing a slightly larger

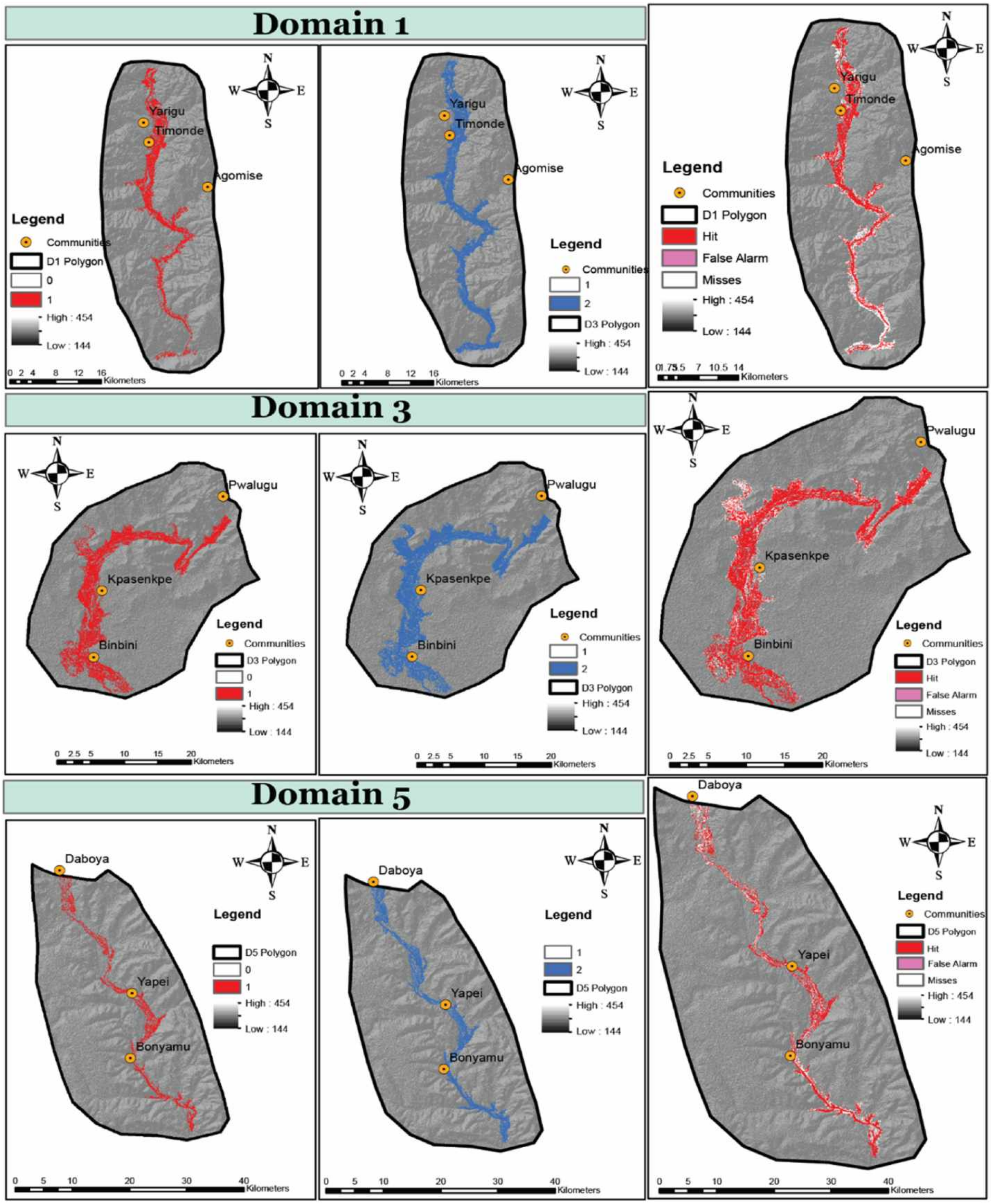

Figure 5 | Spatial comparison of satellite-derived (red) and hydraulic model-simulated (blue) flood extents across Domains 1, 3, and 5, illustrating inundation patterns during the 2020 flood event. Key communities and affected areas are highlighted within each domain.

flooded cropland area than what was detected by the satellite observations. However, despite this modest overestimation, the spatial alignment between the observed and simulated extents is strong, indicating that the model reliably captures the key patterns and magnitude of cropland flooding during the event.

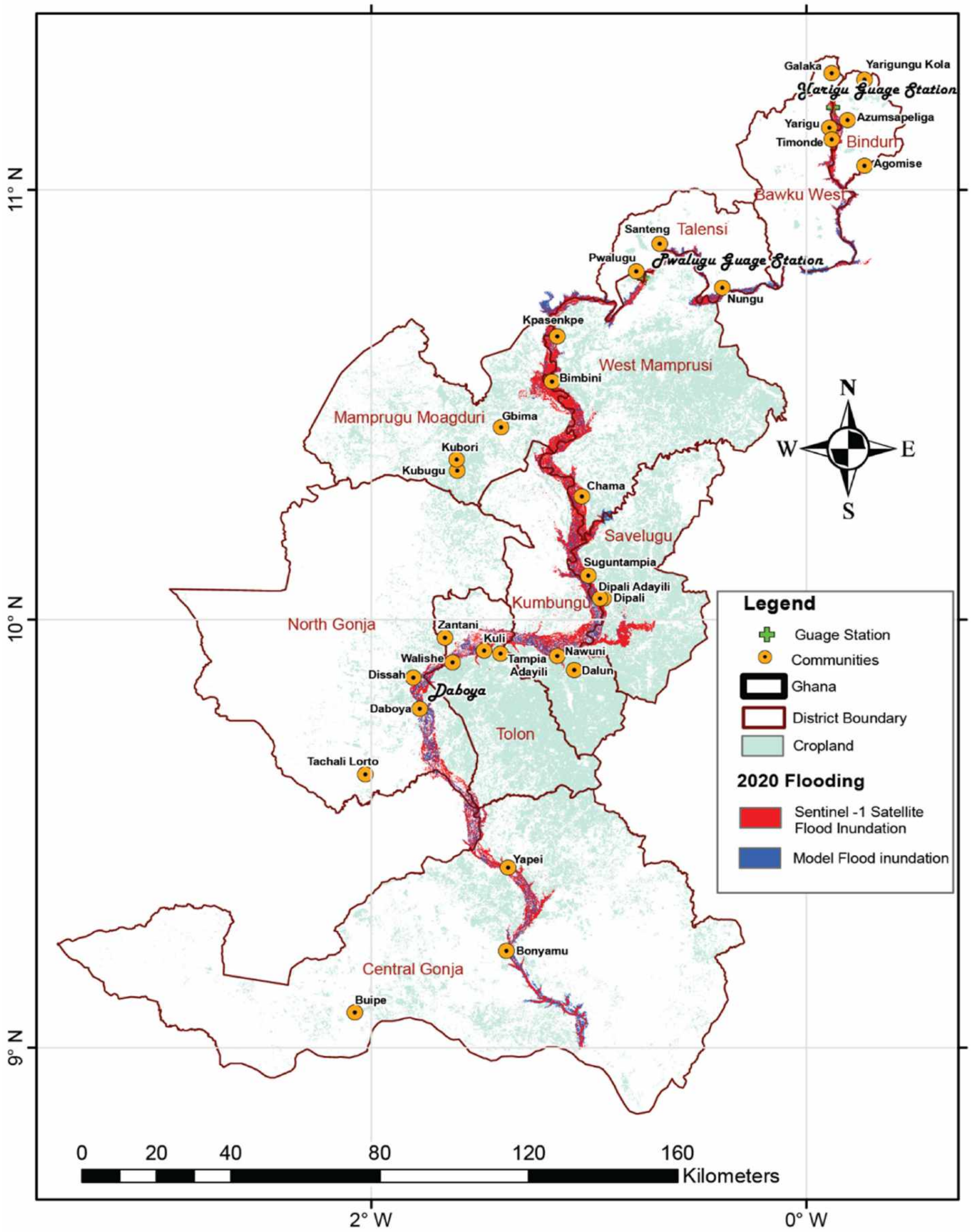

Figure 6 | Flood inundation map of the White Volta Basin for the 2020 event, comparing Sentinel-1 satellite-derived flood extent with model-simulated inundation. The map also shows cropland distribution, district boundaries, gauge stations, and major communities exposed to flooding.

The corresponding district-level statistics (Figure 7) highlight the extent of agricultural vulnerability. Bawku West recorded the highest proportion of flooded cropland (15.66% model; 14.75% satellite), followed by Binduri (11.38% model; 10.68% satellite) and Talensi (5.46% model; 5.27% satellite). Moderate exposure was observed in West Mamprusi and Mamprugu Moagduri, with approximately 3–4% of cropland inundated. In contrast, downstream districts such as Tolon, North Gonja, Central Gonja, and Savelugu recorded less than 2% cropland exposure.

Overall, the strong correspondence between model outputs and satellite observations validates the use of the flood model for assessing inundation dynamics in the basin. More importantly, the results identify critical flood risk hotspots in the upper basin, particularly Bawku West, Binduri, and Talensi, where cropland exposure is most severe. These findings emphasise the importance of targeted flood risk management and early warning interventions to protect agricultural livelihoods in vulnerable districts.

3.4. Flood hazard simulation using the 100-year RP

The 100-year RP design flood, derived using the GEV distribution (Hosking & Wallis 1997) and transformed into a triangular hydrograph following Viessman & Lewis (2003), served as a key input for the HEC-RAS hydraulic model

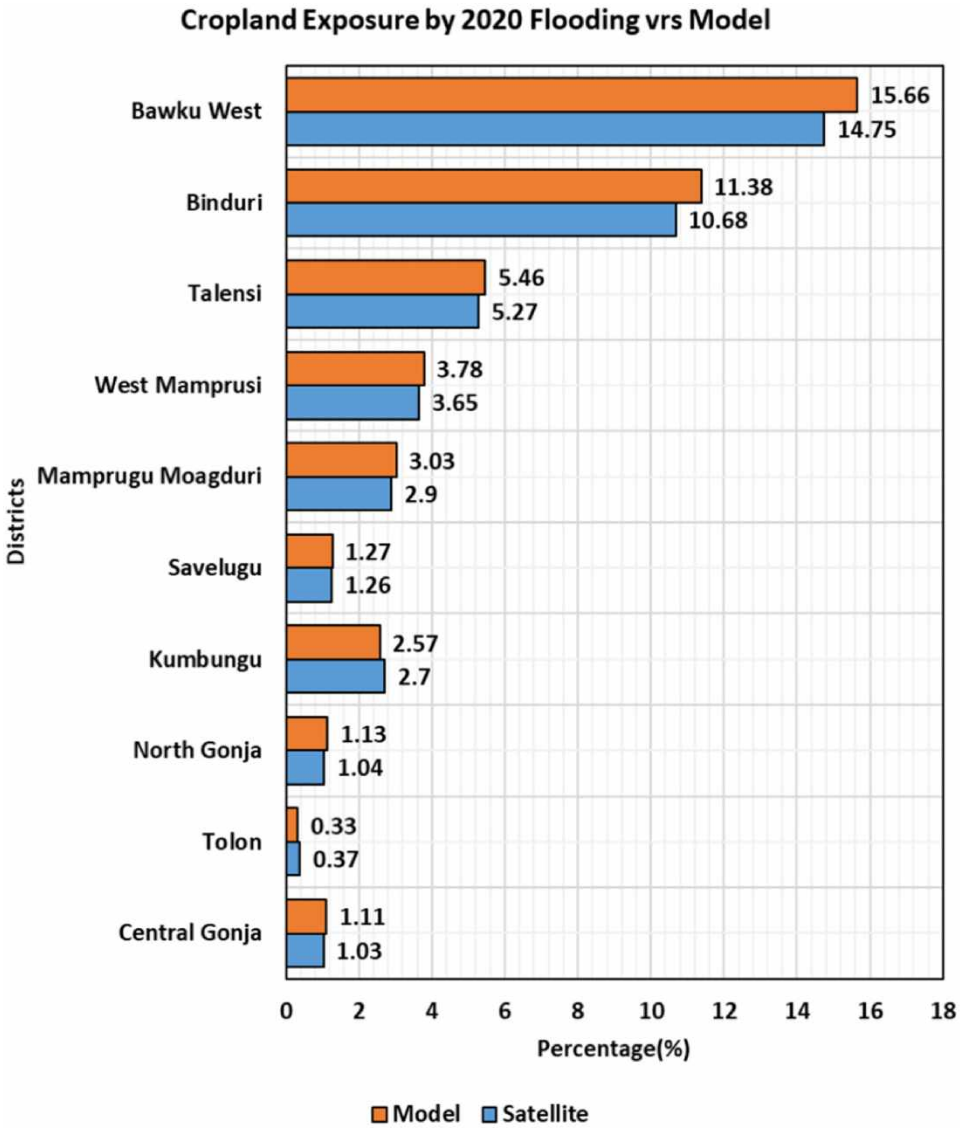

Figure 7 | Comparison of cropland exposure across districts in Northern Ghana during the 2020 flooding event, derived from Sentinel-1 satellite observations and model simulations. The percentages represent the proportion of cropland affected within each district.

(Brunner 2023). Using the 100-year RP is essential because it represents a statistically rare but high-impact flood event that is widely adopted in flood risk management, infrastructure design, and land-use planning.

While the 2020 event provides insight into recent flood dynamics, a 100-year RP scenario enables assessment of potential extreme flooding beyond the range of available observations, especially in data-scarce basins like the White Volta. This allows policymakers and disaster managers to evaluate worst-case but realistic flood conditions, identify high-risk areas, and plan long-term adaptation measures.

The resulting inundation extent is shown in Figure 8, where simulated flooding is overlaid on land-use and land-cover data. The results indicate that large portions of the basin would be submerged during a 100-year flood, reaffirming regional flood susceptibility previously identified (Amisigo *et al.* 2015). Extensive floodplain areas in Binduri, Bawku West, Talensi, West Mamprusi, Tolon, Kumbungu, and Central Gonja emerge as major hotspots. Several communities, such as Yarigu, Azumspalega, Binbini, Kpasenkpe, Kubori, Zantani, Kuli, Dalun, and Yapei, fall directly within the inundation zones, highlighting significant risks to settlements, livelihoods, and critical infrastructure under such an extreme scenario.

Notably, the inundation footprint coincides predominantly with cropland areas, highlighting the potential threat to livelihoods and agricultural productivity. As shown in Figure 9, the cropland exposure analysis indicates that the districts of Bawku West (22.69%) and Binduri (15.08%) experience the highest levels of agricultural land exposure. Other significantly affected districts include Talensi (6.10%), West Mamprusi (6.3%), and Kumbungu (5.6%), while comparatively lower exposures are observed in North Gonja (2.54%), Tolon (1.21%), and Central Gonja (1.49%).

3.5. Flood HI mapping

The integration of hydraulic parameters, specifically water velocity (Figure 10(a)) and inundation depth (Figure 10(b)) for the 100-year RP event yielded a comprehensive flood HI map (Figure 11). The HI map synthesises these individual flood characteristics to depict the spatial variability of combined hazard intensity across the study area, providing a more robust and holistic assessment of potential impacts than either parameter alone (Sampson *et al.* 2015). The spatial configuration of the final HI is directly influenced by the interaction between velocity and depth layers, where areas of deep inundation (>4 m) coincide with high-velocity flow (>1.5 m/s) conditions typically associated with severe flood hazard (Merz *et al.* 2007).

The analysis reveals a pronounced concentration of high-hazard zones along major river corridors and adjacent floodplains. Districts such as West Mamprusi, Bawku West, Binduri, Talensi, Central Gonja, and Kumbungu exhibit extensive areas of elevated HI values, indicating regions where deep flooding and powerful flows converge, thereby posing the greatest potential for damage. The HI map (Figure 11) further highlights critical localities, including Yarigu, Timonde, Nungu, Chama, Binbini, Kpasenkpe, Dipali, Dipali Adayili, Suguntampia, Daboya, and Yapei, where the combined effects of depth and velocity significantly increase risks to communities and agricultural lands. Prolonged inundation in these areas may isolate settlements and devastate crops, while high flow velocities threaten infrastructure stability and soil integrity (Alfieri *et al.* 2015).

The results presented in Table 4 and Figure 12 illustrate a highly uneven distribution of cropland exposure across the basin. Notably, Mamprusi West emerges as the primary hotspot, with 527.7 ha of cropland classified under the extreme hazard category, representing over 75% of the district's total cropland area.

Although other districts, such as Bawku West, Binduri, and Talensi, also record substantial portions of land within the very high and extreme hazard classes, areas such as Savelugu and Mamprugu Moagduri show relatively balanced risk profiles, with larger shares of land within the moderate and high categories.

Nevertheless, the intensity and concentration of risk in Mamprusi West emphasise the need for targeted flood mitigation and climate adaptation strategies to safeguard agricultural assets and ensure food security (Amoako & Boamah 2017).

Croplands situated within high and very high HI zones are exposed to the most destructive flood forces, where scouring from high-velocity flows amplifies the damage caused by prolonged inundation (Gül *et al.* 2010). This integrated hazard approach, moving beyond simple inundation mapping, is essential for prioritising areas for site-specific flood mitigation, including resilient flood defences in high-velocity corridors and climate-smart agricultural practices in flood-prone landscapes.

3.5.1. Hazard classification and agricultural implications

The hazard classification framework (Table 5) provides a structured lens for interpreting flood impacts on croplands within the WVB, linking modelled hazard indices with field-based realities. Hazard levels range from very low (HI < 0.1) to extreme

Figure 8 | Map showing the 100-year return period flood inundation overlaid on land use/land cover in the White Volta Basin, Northern Ghana. The map highlights cropland exposure, major communities, and district boundaries within the floodplain.

(HI > 0.9), defined by increasing water depth, flow velocity, and flood duration (Merz *et al.* 2007; Dottori *et al.* 2016). Beyond hydrodynamic parameters, the framework contextualises these hazard levels in terms of agricultural impacts, institutional responses, and adaptive strategies.

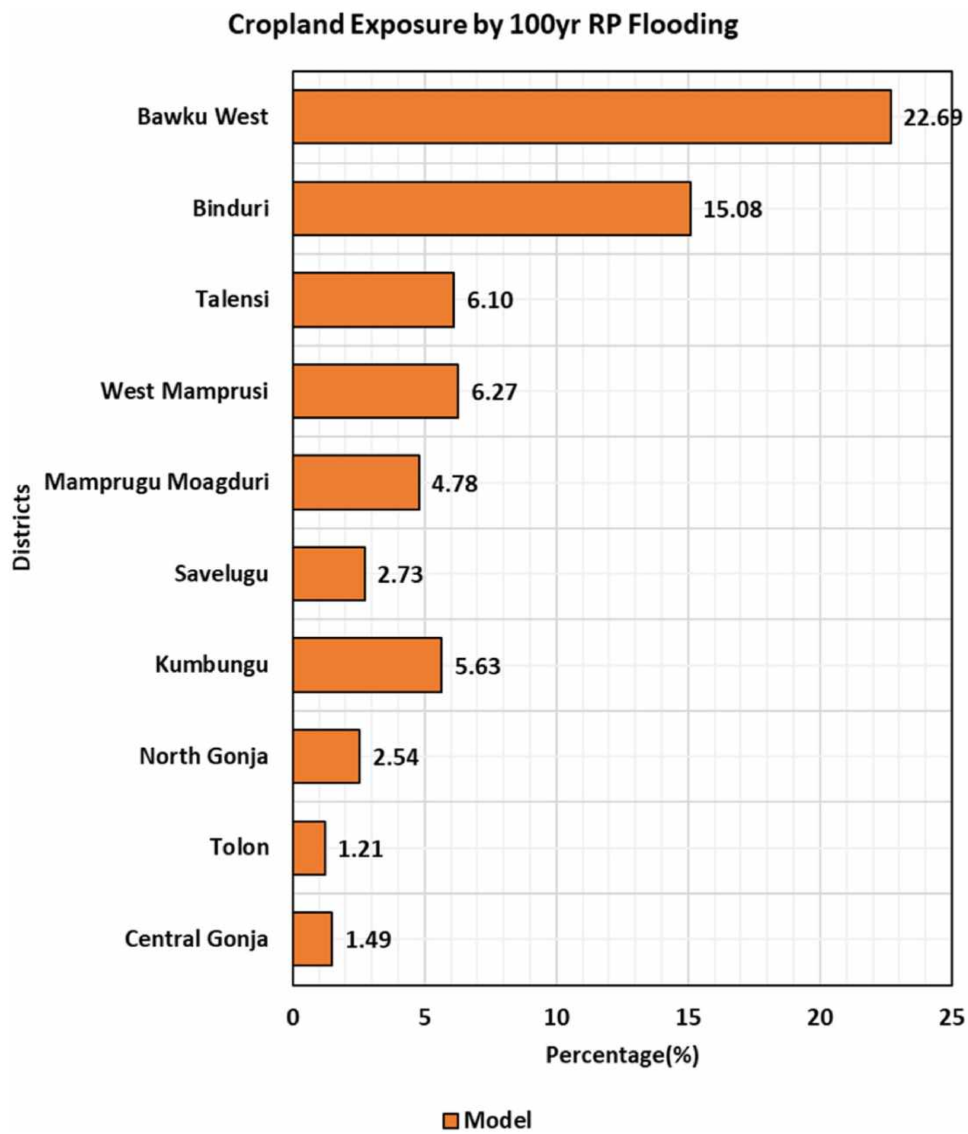

Figure 9 | Cropland Inundation coverage per district for 100-year return period.

At the lower end of the spectrum (very low to low), flooding tends to be shallow and short-lived, often resulting from minor ponding after rainfall events. Rather than being harmful, such flooding can recharge soil moisture and, in some cases, enhance crop productivity. Farmers may even benefit from these mild floods, particularly when supported by nature-based solutions (NBS) such as vegetative bunds and small water-harvesting ponds (Lancaster 2019). Institutional involvement is minimal at this stage, though index-based flood insurance (IBFI) at low premiums can serve as an early resilience mechanism.

As conditions escalate towards the low-sensitive and moderate categories, flood impacts begin to threaten crop establishment and yield. Prolonged submergence and poor drainage can result in seedling mortality, while erosion emerges in mid-floodplain settlements. In such zones, AA based on seasonal forecasts, improved drainage, and agricultural advisories become critical (Coughlan de Perez *et al.* 2016). Institutional responses such as NADMO interventions for input protection and replanting may also be triggered, supported by scaled-up IBFI to cushion losses.

In the high- to very high-hazard classes, floods are often associated with dam releases (e.g., Bagre Dam) coupled with intense rainfall events. These floods cause extensive crop destruction, particularly in rice fields and upland plots. Institutional responses intensify at this stage, involving NADMO-led relocations, MoFA seed replacement programs, and

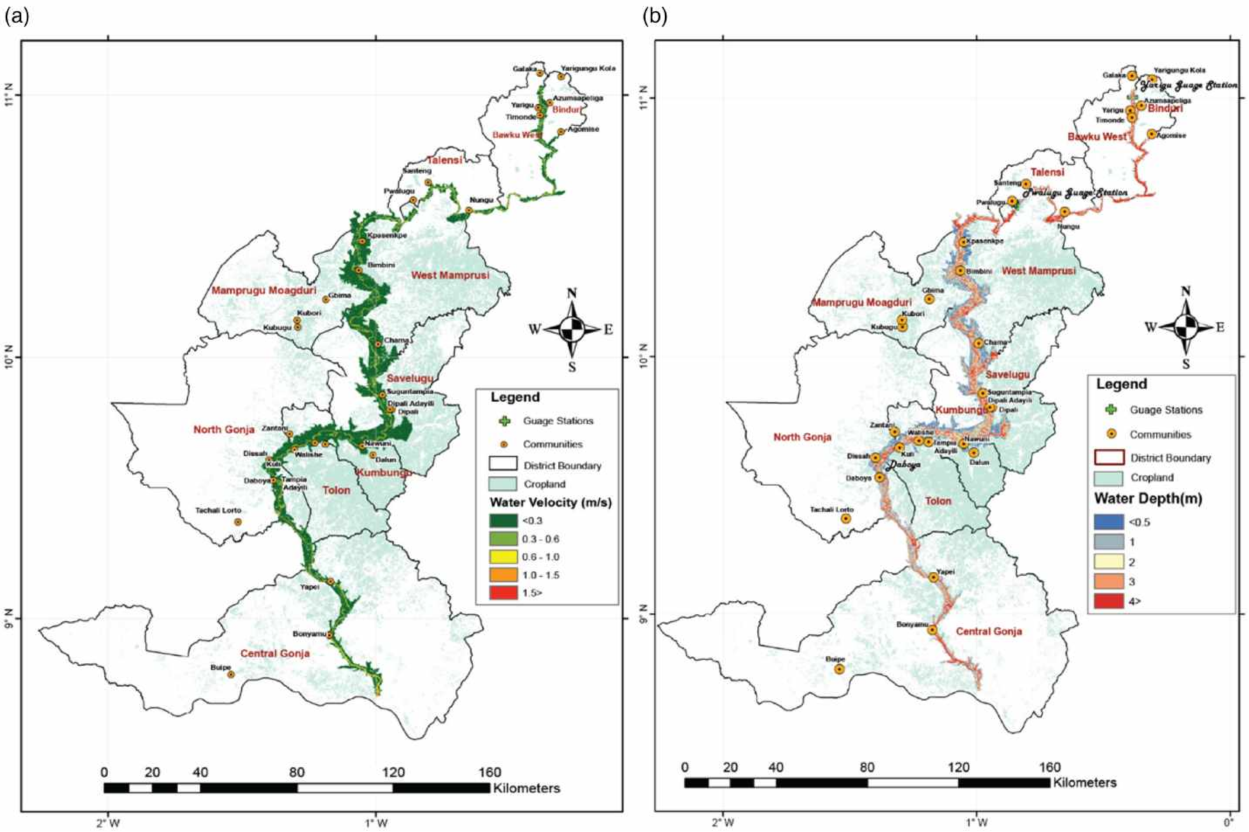

Figure 10 | Simulated water velocities (left) and depth (right) for a 100-year return period flood. The model highlights critical high-velocity zones (>1.5 m/s) posing a risk to cropland, with areas experiencing depths >4 m classified as very high risk.

NGO relief interventions. Enhancing resilience in these zones requires community flood-retention ponds, riparian buffer restoration, and expanded IBFI payouts, which collectively strengthen both immediate recovery and long-term adaptation (Ntim-Amo *et al.* 2022).

The mechanism for decision-making support is codified in the operational trigger column of Table 5, which functions as a trigger-based protocol. By quantifying hydraulic thresholds (depth and velocity) that correspond to specific hazard levels, the framework removes subjective interpretation and provides a non-subjective mandate for resource allocation across different districts in the WVB. For instance, a forecast shifting an area from 'moderate' to 'high' HI serves as a formal trigger for NADMO to pivot from general advisories to physical interventions, such as the protection of community seed banks or relocation assistance. This structured approach ensures that scientific 'flood intelligence' is directly translated into standardised AA, ultimately reducing the systemic vulnerability of agrarian communities across the basin.

Finally, the extreme hazard category (HI > 0.9) corresponds to high-magnitude flood events where water depths exceeded 2 m and velocities surpassed 2 m/s. These events resulted in severe farmland losses, rendered plots unusable for subsequent seasons, and necessitated mass evacuations. Building resilience at this level requires integrated strategies encompassing anticipatory evacuation planning, comprehensive IBFI compensation, and long-term NBS interventions such as wetland restoration, floodplain zoning, and strategic pond networks to enhance adaptive capacity and reduce systemic vulnerability (UNDRR 2022). By linking the HI directly to an 'action' or 'emergency' protocol, the framework provides a non-subjective evidence base for the District Assembly to allocate resources. This represents a transition from descriptive flood mapping to a functional Flood Intelligence System, as visualised in the operational workflow in Figure 13.

3.5.2. Limitations and avenues for future modelling

While the developed HI provides a significant advancement in classifying impact-based flood risk, certain data constraints offer opportunities for future model refinement. For instance, although flood duration is a critical determinant of

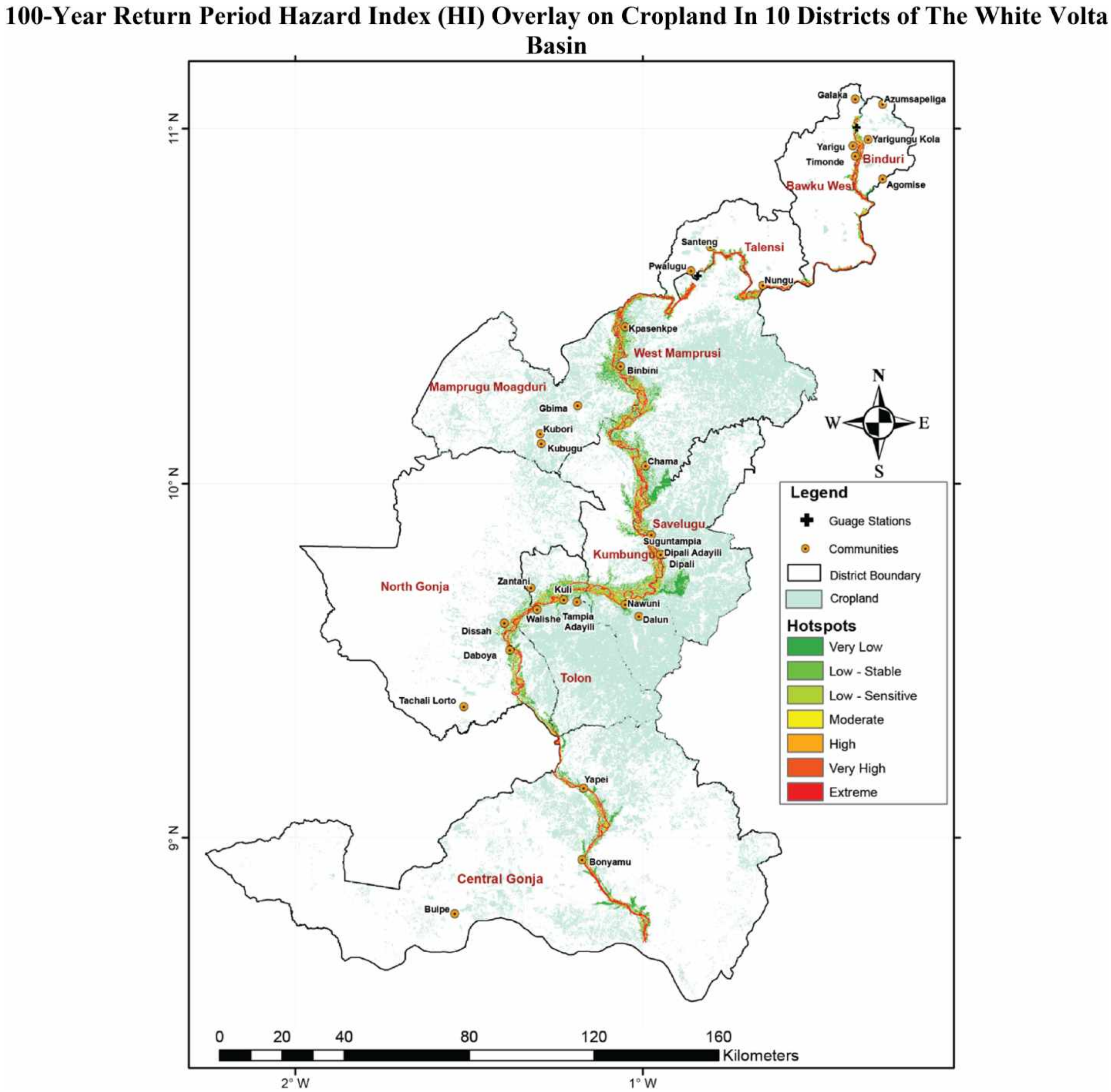

Figure 11 | Map of flood HI for a 100-year return period overlaid on cropland. The results highlight high-risk zones in Bawku West, Binduri, West Mamprusi, Kumbungu, and surrounding settlements like Timonde, Yarigu, Kpasenkpe, and Dipali Adayili, where the combination of high velocity and depth presents a severe threat to agricultural productivity.

crop mortality, the lack of temporally consistent, high-resolution duration data necessitated a focus on the depth–velocity interaction.

Future modelling efforts in the WVB should aim to integrate:

- Flood duration: To capture the physiological impact of prolonged submergence on specific crop types.
- High-resolution topography: Utilising LiDAR-derived DEMs to improve the vertical accuracy of HEC-RAS simulations in low-lying floodplains.
- Socio-economic vulnerability: Coupling hydraulic hazard maps with household-level data (e.g., gender, income, and access to credit) to create a more holistic 'social-hydraulic' risk index.

Table 4 | The classification of the cropland hotspots in hectares per district for 100-year return period

District	Very low (ha)	Low stable (ha)	Low sensitive (ha)	Moderate (ha)	High (ha)	Very high (ha)	Extreme (ha)
Binduri	3.4	2.9	14.7	5.5	15.9	4.6	6.0
Bawku West	9.5	4.0	3.4	5.8	4.8	3.7	17.2
Talensi	10.2	3.4	2.9	5.3	4.4	3.4	15.8
Mamprusi West	89.0	19.3	14.7	22.0	15.8	12.0	527.7
Mamprugu Moagduri	43.7	7.8	5.5	7.6	5.1	3.5	12.8
Kumbungu	79.1	19.6	15.9	23.8	15.5	10.2	41.1
Savelugu	63.2	5.8	4.6	6.9	4.7	3.3	10.2
Tolon	35.2	9.7	6.0	7.4	4.7	3.4	14.4
North Gonja	63.2	12.2	8.5	12.0	8.2	5.9	44.5
Central Gonja	40.9	9.9	6.8	9.4	6.0	4.0	20.2

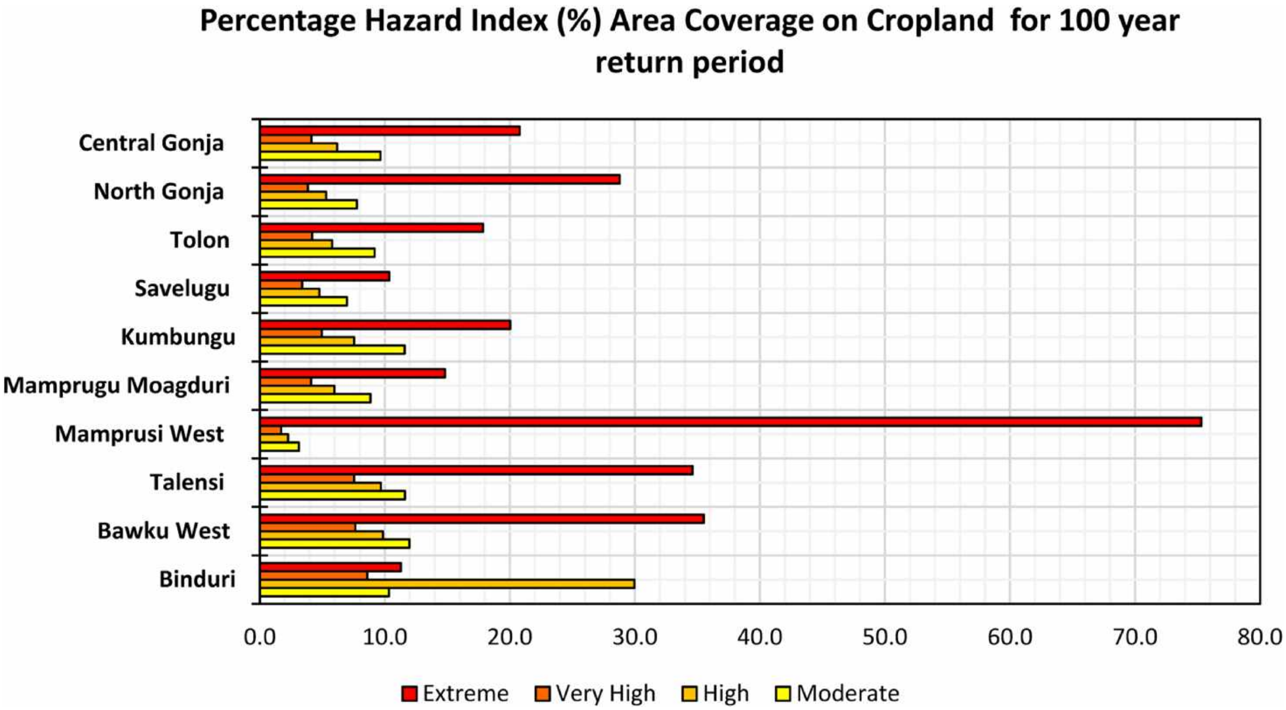

Figure 12 | Bar chart illustrating the percentage hazard index area coverage on cropland across 10 districts for a 100-year return period. Hazard categories include moderate, high, very high, and extreme, with Mamprugu West showing the highest percentage of extreme hazard coverage.

4. MODEL UNCERTAINTY AND SENSITIVITY

The transition from hydraulic simulation to a functional flood intelligence system necessitates a transparent acknowledgement of the uncertainties inherent in the modelling workflow. While the HEC-RAS results provide a robust baseline for the WVB, the following parameters represent the primary sources of potential variance in hazard estimation.

4.1. Manning's roughness (*n*) sensitivity

Flow dynamics in the WVB are highly sensitive to roughness coefficients, which vary significantly between dense riparian vegetation (e.g., Vetiveria nigritana or shrubs) and open seasonal croplands. In this study, Manning's n values were assigned based on standardised hydrological tables (Chow 1959); however, slight variations in these coefficients can shift HI boundaries,

Table 5 | Structured decision-support protocols based on HI thresholds in the WVB

Hazard level	HI range	Practical reality (impact)	Operational trigger and protocol	Primary lead agency
Very low	<0.1	Moisture recharge	*Maintenance protocol*: Routine soil and water conservation (NBS)	MoFA/extension
Low	0.1–0.3	Seedling stress	*Alert protocol*: Advisory for drainage clearance; Index Insurance sign-up	GMet/insurance
Moderate	0.3–0.5	Erosion onset	*Action protocol 1*: Targeted salvage harvesting; input relocation to highlands	NADMO/MoFA
High	0.5–0.7	Major crop loss	*Action protocol 2*: Livestock evacuation; seed bank protection; partial IBFI payouts	NADMO/NGOs
Very high	0.7–0.9	Destruction	*Emergency protocol 1*: Mandatory human evacuation; activation of relief centers	District assembly
Extreme	>0.9	2020-scale event	*Emergency protocol 2*: Full-scale disaster response; total loss compensation via IBFI	WRC/NADMO

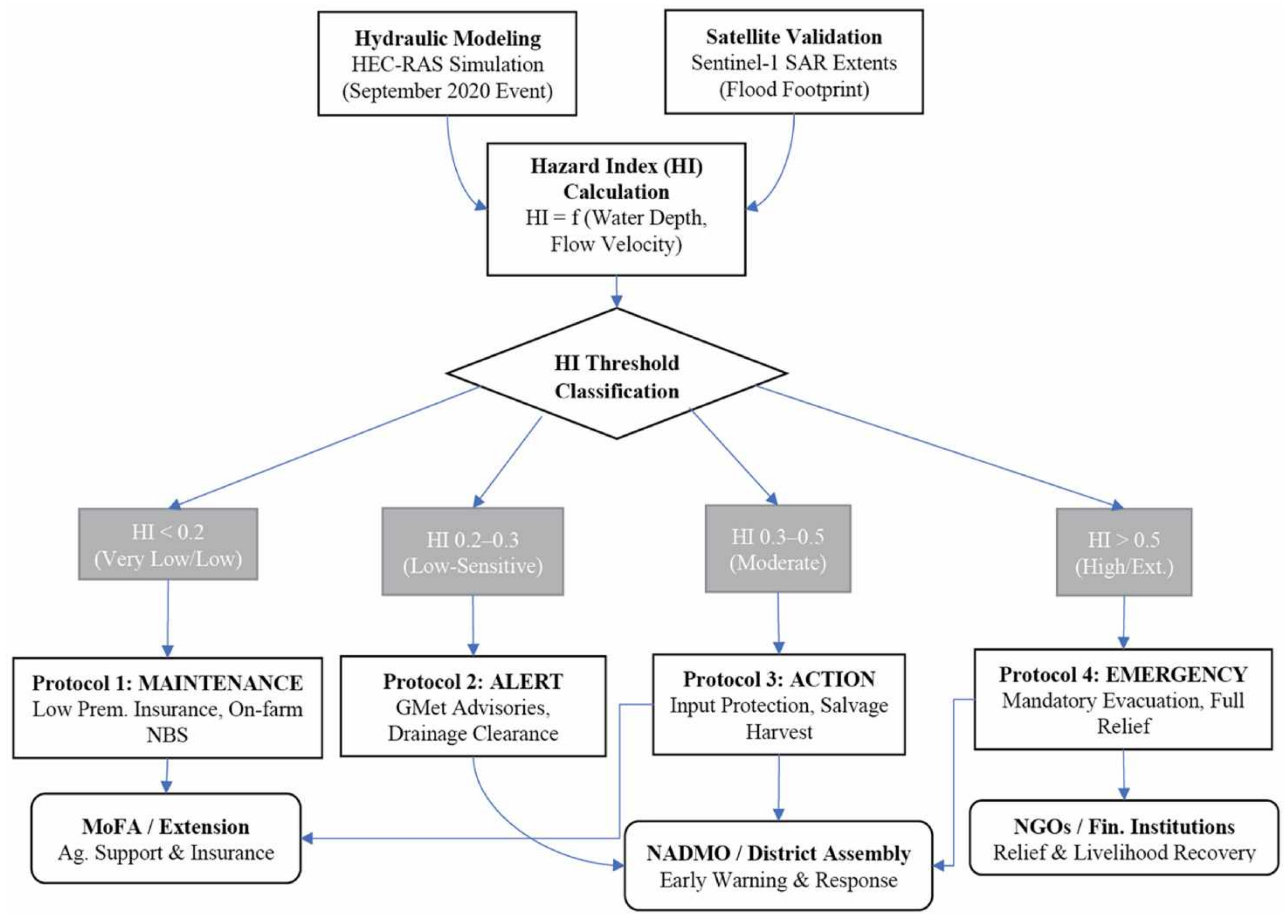

Figure 13 | Operational flowchart for the trigger-based decision-support system.

particularly the flow velocity component. Higher roughness values tend to increase simulated water depths while attenuating velocities, potentially altering the HI classification in steep-sloped or narrow channel reaches (Bhola *et al.* 2019).

4.2. DEM vertical error and inundation accuracy

In low-gradient, relatively flat floodplains like those of the White Volta, vertical errors in the DEM can significantly influence the simulated inundation footprint, where even minor vertical inaccuracies (e.g., ±1 m) can lead to substantial lateral shifts in flood extent (Sampson *et al.* 2016). Consequently, refined DEMs, ideally those integrating high-resolution LiDAR data, are essential for robust flood modelling, as they significantly reduce the potential for topographical errors to compromise the integrity of flood risk assessments (Podhorányi *et al.* 2011; Smart 2018). To mitigate the impact of these inherent topographical uncertainties, the model was validated against Sentinel-1 SAR-derived extents. While this cross-verification aligns the simulated hazard with physical observations from the 2020 event, the validation yielded a fuzzy accuracy below 80%. This performance level is partly attributable to the temporal resolution limitations of Sentinel-1, which may miss peak flood moments. Therefore, it is advisable to adopt realistic, context-aware performance expectations, acknowledging that while the model effectively 'ground-truths' hazard zones, it remains constrained by the available satellite and topographic data.

4.3. Boundary condition and discharge uncertainty

Uncertainty in upstream discharge and the precise timing of the Bagre Dam spillway releases introduces potential bias in peak flow estimation. In transboundary basins with inconsistent gauge records, these boundary conditions represent a significant challenge. By utilising the catastrophic September 2020 event as a benchmark, this study leveraged the highest available quality of historical gauge data and satellite observations to minimise discharge-related errors, ensuring the modelled peaks represent a 'worst-case' operational scenario.

4.4. HI threshold sensitivity

The classification of the HI into discrete levels (e.g., 'moderate' to 'high') involves thresholds calibrated to physical crop damage (e.g., rice submergence tolerance and maize lodging). We acknowledge that a 10–15% variance in these HI thresholds, whether due to different crop varieties or soil types, would alter the total identified 'high-risk' acreage. Consequently, these indices are presented as a science-to-policy framework designed to guide resource prioritisation, rather than as static, absolute predictions.

4.5. Synthesis for decision-support

Despite these inherent uncertainties, the integration of hydraulic modelling with satellite validation provides a standardised, non-subjective evidence base for disaster risk management. The sensitivity of the model does not undermine the validity of the operational protocols (Table 5); rather, it emphasises the importance of using the HI as a dynamic tool that should be periodically recalibrated as higher-resolution topographical data and updated transboundary flow records become available.

5. CONCLUSION

This study demonstrated the effectiveness of the HEC-RAS 2D hydrodynamic model in accurately simulating the September 2020 flood event in the WVB, confirming its suitability for basin-scale flood hazard assessment and exposure analysis. Calibration and validation using Sentinel-1 SAR-derived flood extents showed high spatial agreement across the study domains, particularly in Domain 3, highlighting the model's robustness in capturing local hydraulic dynamics and floodplain behaviour.

The cropland exposure assessment revealed significant agricultural vulnerability, especially in upper basin districts such as Mamprusi West, Bawku West, Binduri, and Talensi, where over 15% of cultivated areas were inundated. Integrating flood depth and velocity into a composite flood HI enabled the classification of hazard levels from very low to extreme, effectively linking hydrodynamic thresholds with observed crop impacts. The framework illustrates that while low-intensity flooding can enhance soil moisture and short-term productivity, moderate to extreme floods lead to extensive crop damage, soil erosion, and livelihood disruptions.

The flood HI framework, therefore, provides an operational tool that bridges hydrodynamic modelling with field-level agricultural realities, offering a scientifically grounded basis for targeted early warning systems, IBFI schemes, and the design of NBS. These outputs have direct relevance for national institutions such as NADMO, MoFA, WRC, and GMet, supporting the development of AA and spatially tailored agricultural advisories.

Beyond technical validation, the study underscores the need for integrated flood governance and transboundary coordination within the WVB. The influence of upstream dam operations and land-use changes on downstream flood dynamics highlights a critical control on flood hazard that warrants focused investigation. In this regard, the findings of this study provide the hydrodynamic and exposure baseline for a companion and ongoing line of research that explicitly examines the role of upstream reservoir operations and climate-driven inflows in shaping food, as well as the translation of climate information services to last-mile users.

In summary, this research establishes HEC-RAS as a robust and scalable framework for flood hazard and exposure analysis in Ghana, advancing data-driven and climate-resilient planning. Future work should integrate climate change projections, socio-economic exposure and vulnerability mapping, upstream dam operation scenarios, and adaptive management strategies, alongside strengthened climate information service dissemination, to enhance basin-wide flood resilience and decision-making.

Future refinements of this modelling framework should consider the integration of additional dynamic variables to enhance predictive accuracy and policy relevance. Key among these are high-resolution land-cover changes, which influence hydraulic roughness and runoff dynamics, and antecedent soil moisture conditions, which dictate the basin's threshold for saturation-excess flooding. Furthermore, incorporating crop-specific phenological data would allow the HI to account for seasonal sensitivity, such as the increased vulnerability of rice during the flowering stage versus the ripening stage.

Crucially, the framework should evolve to explicitly derive flood duration by integrating key temporal and spatial variables, including hydrograph recession rates, localised micro-topographic ponding effects, and time-series satellite observations. Such integrations would facilitate the transition from static hazard mapping to a real-time, impact-based forecasting system for the WVB, providing a more granular understanding of how long specific agricultural zones remain inundated.

ACKNOWLEDGEMENT

This study was made possible through the support of the Pan-African and Transdisciplinary Lens on the Margins: Tackling the Risks of Extreme Events (PALM-TREEs) project, funded by UK aid from the UK government and by the International Development Research Centre, Ottawa, Canada, as part of the Climate Adaptation and Resilience (CLARE) research programme (Grant Number 110002-001). The views expressed herein do not necessarily represent those of the UK government, IDRC, or its Board of Governors.

AUTHOR CONTRIBUTIONS

Samuel Owusu Ansah led the study's conceptualisation, methodology, investigation, data curation, visualisation, and manuscript drafting. Yakob Umer contributed substantially to conceptual and methodological design, including alignment with the PALM TREE's framework, and led the HEC-RAS model setup, calibration, validation, and analysis. Joshua Asamoah and Alfred Awuah contributed to data curation. Thompson Annor, Andrew Manoba Limantol, and Isaac Larbi supervised, reviewed, and edited the manuscript to ensure PALM TREE's alignment. Meron Teferi Taye provided methodological guidance and critical review, particularly on PALM TREE's alignment. Babatunde Abiodun contributed to scientific oversight. All authors approved the final manuscript.

DATA AVAILABILITY STATEMENT

All relevant data are included in the paper or its Supplementary Information.

CONFLICT OF INTEREST

The authors declare there is no conflict. During the preparation of this work, the author(s) used ChatGPT to correct grammatical constructions. After using this tool/service, the author(s) reviewed and edited the content as needed and take(s) full responsibility for the content of the publication.

REFERENCES

Afzal, M. A., Ali, S., Nazeer, A., Khan, M. I., Waqas, M. M., Aslam, R. A., Cheema, M. J. M., Nadeem, M., Saddique, N., Muzammil, M. & Shah, A. N. (2022) Flood inundation modeling by integrating HEC-RAS and satellite imagery: a case study of the Indus River Basin, *Water (Switzerland)*, **14** (19), 2984. https://doi.org/10.3390/w14192984.

Alfieri, L., Burek, P., Feyen, L. & Forzieri, G. (2015) Global warming increases the frequency of river floods in Europe, *Hydrology and Earth System Sciences*, **19** (5), 2247–2260. https://doi.org/10.5194/hess-19-2247-2015.

Amisigo, B. A., McCluskey, A. & Swanson, R. (2015) Modeling impact of climate change on water resources and agriculture demand in the Volta Basin and other basin systems in Ghana, *Sustainability*, **7** (6), 6957–6975. https://doi.org/10.3390/su7066957.

Amoako, C. & Boamah, E. F. (2017) The three-dimensional causes of flooding in Accra, Ghana, *International Journal of Urban Sustainable Development*, **7** (1), 109–129. https://doi.org/10.1080/19463138.2014.984720.

Amoussou, E., Lawin, A. E., Afouda, A. & Tramblay, Y. (2024) Hydraulic modeling for flood risk assessment in the Ouémé Basin, Benin, *Natural Hazards*, **120** (2), 1533–1553. https://doi.org/10.5194/piahs-385-141-2024.

Apel, H., Aronica, G. T., Kreibich, H. & Thieken, A. H. (2009) Flood risk analyses – how detailed do we need to be?, *Natural Hazards*, **49** (1), 79–98. https://doi.org/10.1007/s11069-008-9277-8.

Arhin, C. A. & Frimpong, D. O. (2025) Climate-induced displacement and its implications on human security: a case study of Ghana, *International Journal of Research and Innovation in Applied Science (IJRIAS)*, **10** (11), 105–120. https://doi.org/10.51584/IJRIAS.2025.101100011.

Aronica, G. T., Bates, P. D. & Horritt, M. S. (2002) Assessing the uncertainty in distributed model predictions using observed binary pattern information within GLUE, *Hydrological Processes*, **16** (10), 2001–2016. https://doi.org/10.1002/hyp.398.

Atanga, R. A. & Tankpa, V. (2021) Climate change, flood disaster risk and food security nexus in Northern Ghana, *Frontiers in Sustainable Food Systems*, **5**, 706721. https://doi.org/10.3389/fsufs.2021.706721.

Atubiga, J. A. & Donkor, E. (2022) Exploring the impact of floods on rural communities on emerging food security challenges in Ghana, *Journal of Social Sciences*, **18** (1), 191–200. https://doi.org/10.3844/jssp.2022.191.200.

Barry, B., Obuobie, E., Andreini, M., Andah, W. & Pluquet, M. (2005) The Volta River basin. *Comparative Study of River Basin Development and Management. Rapport, IWMI, CAWMA*.

Bhola, P. K., Leandro, J. & Disse, M. (2019) Reducing uncertainties in flood inundation outputs of a two-dimensional hydrodynamic model by constraining roughness, *Natural Hazards and Earth System Sciences*, **19** (7), 1445–1457. https://doi.org/10.5194/nhess-19-1445-2019.

Braun, A. (2021) Retrieval of digital elevation models from Sentinel-1 radar data: open applications, techniques, and limitations, *Open Geosciences*, **13** (1), 532–569. https://doi.org/10.1515/geo-2020-0246.

Brunner, G. W. (2023) *HEC-RAS River Analysis System User's Manual (Version 6.3)*. Davis, CA: U.S. Army Corps of Engineers, Hydrologic Engineering Center.

Chow, V. T. (1959) *Open-Channel Hydraulics*. New York: McGraw-Hill.

Coughlan de Perez, E., van den Hurk, B., van Aalst, M. K., Amuron, I., Bamanya, D., Hauser, T., Jongma, B., Lopez, A., Mason, S., Mendler de Suarez, J., Pappenberger, F., Rueth, A., Stephens, E., Suarez, P., Wagemaker, J. & Zsoter, E. (2016) Action-based flood forecasting for early warning and response, *Hydrology and Earth System Sciences*, **20** (9), 3549–3560. https://doi.org/10.5194/hess-20-3549-2016.

De Luca, G., Silva, J. M. N., Di Fazio, S. & Modica, G. (2022) Integrated use of Sentinel-1 and Sentinel-2 data and open-source machine learning algorithms for land cover mapping in a Mediterranean region, *European Journal of Remote Sensing*, **55** (1), 52–70. https://doi.org/10.1080/22797254.2021.2018667.

Dembélé, M., Oriani, F., Tumbulto, J., Mariéthoz, G. & Schaefli, B. (2019) Gap-filling of daily streamflow time series using Direct Sampling in various hydroclimatic settings, *Journal of Hydrology*, **569**, 573–586. https://doi.org/10.1016/j.jhydrol.2018.11.076.

Dembélé, M., Hrachowitz, M., Savenije, H. H. G., Mariéthoz, G. & Schaefli, B. (2020) Improving the predictive skill of a distributed hydrological model by calibration on spatial patterns with multiple satellite data sets, *Water Resources Research*, **56** (2), e2019WR026085. https://doi.org/10.1029/2019WR026085.

Di Baldassarre, G., Castellarin, A. & Brath, A. (2010) Analysis of the effects of levee heightening on flood propagation: example of the River Po, Italy, *Hydrological Sciences Journal*, **54** (6), 1007–1017. https://doi.org/10.1623/hysj.54.6.1007.

Dottori, F., Salamon, P., Bianchi, A., Alfieri, L., Hirpa, F. A. & Feyen, L. (2016) Development and evaluation of a framework for global flood hazard mapping, *Advances in Water Resources*, **94**, 87–102. https://doi.org/10.1016/j.advwatres.2016.05.002.

Dutta, D., Herath, S. & Musiake, K. (2003) A mathematical model for flood loss estimation, *Journal of Hydrology*, **277** (1–2), 24–49. https://doi.org/10.1016/S0022-1694(03)00084-2.

Fiasorgbor, D., Wiafe, E., Tettey, C. & Abasiyam, M. (2018) Assessment of the coping strategies of flood victims in the Builsa District, *American Journal of Environmental Science and Engineering*, **2** (1), 17–25. https://doi.org/10.11648/j.ajese.20180201.12.

Ghansah, B., Forkuo, E. K., Osei, E. F., Appoh, R. K., Asare, M. Y. & Klutse, N. A. B. (2018) Mapping the spatial distribution of small reservoirs in the White Volta Sub-basin of Ghana, *Remote Sensing Applications: Society and Environment*, **9**, 107–115. https://doi.org/10.1016/j.rsase.2017.12.003.

Glago, F. J. (2021) Flood disaster hazards: causes, impacts and management – a state-of-the-art review. In: *Natural Hazards – Impacts, Adjustments and Resilience*. London, UK: IntechOpen, pp. 21–38. https://doi.org/10.5772/intechopen.95048.

Gül, G. O., Harmancıoğlu, N. & Gül, A. (2010) A combined hydrologic and hydraulic modeling approach for testing efficiency of structural flood control measures, *Natural Hazards*, **54** (2), 245–260. https://doi.org/10.1007/s11069-009-9464-2.

Horritt, M. S. & Bates, P. D. (2002) Evaluation of 1D and 2D numerical models for predicting river flood inundation, *Journal of Hydrology*, **268** (1–4), 87–99. https://doi.org/10.1016/S0022-1694(02)00121-X.

Hosking, J. R. M. & Wallis, J. R. (1997) *Regional Frequency Analysis*: *An Approach Based on L-Moments*. Cambridge, UK: Cambridge University Press.

Komi, K., Neal, J., Trigg, M. A. & Diekkrüger, B. (2017) Modelling of flood hazard extent in data-sparse areas: a case study of the Oti River Basin, West Africa, *Journal of Hydrology: Regional Studies*, **10**, 122–132. https://doi.org/10.1016/j.ejrh.2017.03.001.

Kwarteng, P., Nyaaba, E., Honlah, E., Serbeh, R. & Abass, K. (2025) Living with familiar hazards: flood experiences of urban households and health implications in Ghana, *Environmental Hazards*. Advance online publication. https://doi.org/10.1080/17477891.2025.2534643.

Lancaster, B. (2019) *Rainwater Harvesting for Erylands and Beyond*, Volume 2 (2nd ed.), Water-Harvesting Earthworks. Tucson, AZ: Rainsource Press. ISBN: 978-0977246441.

Logah, F. Y., Osei, F. B., Kankam-Yeboah, K. & Adjei, K. A. (2017) Application of HEC-RAS model for flood forecasting in the Lower Volta Basin of Ghana, *Regional Studies*, **14**, 1–9. https://doi.org/10.1016/j.ejrh.2017.09.002.

Merz, B., Thieken, A. H. & Gocht, M. (2007) Flood risk mapping at the local scale: concepts and challenges, *Natural Hazards and Earth System Sciences*, **7** (5), 545–556. https://doi.org/10.1007/978-1-4020-4200-3_13.

Ntim-Amo, G., Yin, Q., Ankrah, E. K., Liu, Y., Ankrah Twumasi, M., Agbenyo, W., Xu, D., Ansah, S., Mazhar, R. & Gamboc, V. K. (2022) Farm households' flood risk perception and adoption of flood disaster adaptation strategies in northern Ghana, *International Journal of Disaster Risk Reduction*, **80**, 103223. https://doi.org/10.1016/j.ijdrr.2022.103223.

Pérez-Hoyos, A., Rembold, F., Kerdiles, H. & Gallego, J. (2017) Comparison of global land cover datasets for cropland monitoring, *Remote Sensing*, **9** (11), 1118. https://doi.org/10.3390/rs9111118.

Podhorányi, M., Unucka, J., Bobál, P. & Říhová, V. (2011) Effects of LIDAR DEM resolution in hydrodynamic modelling: model sensitivity for cross-sections, *International Journal of Digital Earth*, **6** (1), 3–27. https://doi.org/10.1080/17538947.2011.596578.

Rahman, A., Haddad, K., Haque, M., Kuczera, G. & Weinmann, P. (2015) Australian rainfall and runoff project 5: regional flood methods: stage 3 report. Commonwealth of Australia (Geoscience Australia): Canberra, Australia. Available at: https://arr.ga.gov.au/__data/assets/pdf_file/0004/40549/ARR_Project-5_Stage-3_report.pdf.

Sampson, C. C., Smith, A. M., Bates, P. D., Neal, J. C., Alfieri, L. & Freer, J. E. (2015) A high-resolution global flood hazard model, *Water Resources Research*, **51** (9), 7358–7381. https://doi.org/10.1002/2015WR016954.

Sampson, C. C., Smith, A. M., Bates, P. D., Neal, J. C. & Trigg, M. A. (2016) Perspectives on open access high resolution digital elevation models to produce global flood hazard layers, *Frontiers in Earth Science*, **3**, 85. https://doi.org/10.3389/feart.2015.00085.

Schumann, G., Bates, P. D., Horritt, M. S. & Matgen, P. (2009) Progress in integration of remote sensing–derived flood extent and stage data and hydraulic models, *Reviews of Geophysics*, **47**, RG4001. https://doi.org/10.1029/2008RG000274.

Smart, G. (2018) LiDAR resolution for catchment-inclusive hydrodynamic models, *E3S Web of Conferences*, **40**, 06031. https://doi.org/10.1051/e3sconf/20184006031.

Smits, W. K., Attoh, E. M. N. A. N. & Ludwig, F. (2024) Flood risk assessment and adaptation under changing climate for the agricultural system in the Ghanaian White Volta Basin, *Climatic Change*, **177** (3), Article 39. https://doi.org/10.1007/s10584-024-03694-6.

Stephens, E. M., Bates, P. D., Freer, J. E. & Mason, D. C. (2014) The impact of uncertainty in satellite data on the assessment of flood inundation models, *Hydrological Processes*, **28** (2), 462–478. https://doi.org/10.1016/j.jhydrol.2011.10.040.

Teng, J., Jakeman, A. J., Vaze, J., Croke, B. F. W., Dutta, D. & Kim, S. (2017) Flood inundation modelling: a review of methods, recent advances and uncertainty analysis, *Environmental Modelling & Software*, **90**, 201–216. https://doi.org/10.1016/j.envsoft.2017.01.006.

UNDRR (2022) *Global Assessment Report on Disaster Risk Reduction 2022: Our World at Risk*. Geneva, Switzerland: United Nations Office for Disaster Risk Reduction.

U.S. Army Corps of Engineers (USACE) (2016) *HEC-RAS River Analysis System: User's Manual (Version 5.0)*. Davis, CA: Hydrologic Engineering Center.

Viessman, W. & Lewis, G. L. (2003) *Introduction to Hydrology*, 5th edn. Upper Saddle River, NJ: Prentice Hall.

Willis, T. D. M., Smith, M. W., Cross, D. E., Hardy, A. J., Ettrich, G. E., Malawo, H., Chalo, C., Sinkombo, M. & Thomas, C. J. (2022) Hydrodynamic modeling of inundation patterns of a large African floodplain indicates sensitivity to waterway restoration, *Water Resources Research*, **58** (11), e2021WR030107. https://doi.org/10.1029/2021WR030107.

Yiran, G. A. B. & Stringer, L. C. (2016) Spatio-temporal analyses of impacts of multiple climatic hazards in a savannah ecosystem of Ghana, *Climate Risk Management*, **14**, 11–26. https://doi.org/10.1016/j.crm.2016.09.003.

First received 25 December 2025; accepted in revised form 20 May 2026. Available online 18 June 2026